Higher-Order Mean-Motion Resonances Can Form in Type-I Disk Migration

Finnegan M. Keller,[1, 2] Fei Dai,[2, 3, 4] and Wenrui Xu[5]

[1]*Department of Physics, Brown University, Providence, RI 02912, USA*
[2]*Institute for Astronomy, University of Hawai'i, 2680 Woodlawn Drive, Honolulu, HI 96822, USA*
[3]*Division of Geological and Planetary Sciences, 1200 E California Blvd, Pasadena, CA, 91125, USA*
[4]*Department of Astronomy, California Institute of Technology, Pasadena, CA 91125, USA*
[5]*Center for Computational Astrophysics, Flatiron Institute, New York, USA*

ABSTRACT

Type-I disk migration can form a chain of planets engaged in first-order mean-motion resonances (MMRs) parked at the disk inner edge. However, while second- or even third-order resonances were deemed unlikely due to their weaker strength, they have been observed in some planetary systems (e.g. TOI-178 bc: 5:3, TOI-1136 ef: 7:5, TRAPPIST-1 bcd: 8:5-5:3). We performed $> 6,000$ Type-I simulations of multi-planet systems that mimic the observed *Kepler* sample in terms of stellar mass, planet size, multiplicity, and intra-system uniformity over a parameter space encompassing transitional and truncated disks. We found that Type-I migration coupled with a disk inner edge can indeed produce second- and third-order resonances (in a state of libration) in $\sim 10\%$ and 2% of resonant-chain systems, respectively. Moreover, the fraction of individual resonances in our simulations reproduced that of the observed sample (notably, 5:3 is the most common second-order MMR). The formation of higher-order MMRs favors slower disk migration and a smaller outer planet mass. Higher-order resonances do not have to form with the help of a Laplace-like three-body resonance as was proposed for TRAPPIST-1. Instead, the formation of higher-order resonance is assisted by breaking a pre-existing first-order resonance, which generates small but non-zero initial eccentricities ($e \approx 10^{-3}$ to 10^{-2}). We predict that 1) librating higher-order resonances have higher equilibrium e (~ 0.1); 2) be more likely found as an isolated pair in an otherwise first-order chain; 3) more likely emerge in the inner pairs of a chain.

1. INTRODUCTION

There is mounting evidence (e.g. Mills et al. 2016; Izidoro et al. 2017; Leleu et al. 2021; Dai et al. 2023; Luque et al. 2023; Dai et al. 2024; Hamer & Schlaufman 2024) that Kepler-like planets (~ 0.1AU, $< 4R_\oplus$, $N_p \geq 3$, Winn & Fabrycky 2015; Zhu & Dong 2021) could have formed initially in chains of mean-motion resonance (MMR) through Type-I (non-gap-opening) convergent disk migration (Goldreich & Tremaine 1979; Ward 1997; Lin & Papaloizou 1986; Kley & Nelson 2012;

Izidoro et al. 2017; Ogihara et al. 2018; Wong & Lee 2024). After the gas disk dissipates, the stability of a planetary system is no longer protected by eccentricity and inclination damping induced by planet-disk interactions (Papaloizou & Larwood 2000). Over time, orbital instability or other dynamical effects disrupt the initial resonances, leading to the predominantly non-resonant orbital architectures observed among mature Kepler-like planets (Pichierri & Morbidelli 2020; Goldberg & Batygin 2022; Izidoro et al. 2017; Goldberg et al. 2022; Li et al. 2024; Matsumoto et al. 2012; Rath et al. 2022).

The order of an MMR is defined by the difference of two integers involved ($|p - q|$, e.g. 3:2 is first-order, 5:3 is second-order, 8:5 is third-order). While the distinc-

Corresponding author: Finnegan Keller
finnegan_keller@brown.edu

tion may appear trivial at first, a careful treatment of the resonant Hamilton (Murray & Dermott 1999; Hadden 2019a) shows that the strength of the MMR scales as orbital eccentricity raised to the power of the order ($\propto e^{|p-q|}$). This is mostly because the perturbation near conjunctions in higher-order resonance partially cancel out (Tamayo & Hadden 2024). For most Kepler-like planetary systems, the orbital eccentricity is low ($\lesssim 0.05$ e.g. Hadden & Lithwick 2017; Xie et al. 2016), so higher-order resonance could be more than an order of magnitude weaker than first-order resonance. Acting as a weak link in a chain of mean-motion resonances, higher-order MMR may play a role in the disruption of initially resonant Kepler-like systems (Dai et al. 2023).

Unless characterizing a specific system with an apparent higher-order resonance(s) (MacDonald et al. 2016; Mills et al. 2016; Siegel & Fabrycky 2021; MacDonald et al. 2016; Quinn & MacDonald 2023; Lammers & Winn 2024; Dai et al. 2023; Tamayo et al. 2017; Coleman et al. 2019), previous disk migration simulations usually overlooked higher-order MMR as capturing planets into weaker higher-order resonances was assumed to be much more difficult than first-order MMR. Pioneering works by Xiang-Gruess & Papaloizou (2015); Xu & Lai (2017) showed that capturing a pair of planets into second-order resonances requires more specific circumstances but is still possible. Higher-order MMR formation mandates convergent migration, a slower migration rate, near-unity planet-planet mass ratios, and low (but not zero, see Section 4.7) pre-resonance eccentricities (Xu & Lai 2017; Batygin 2015). A number of multi-planet planetary systems contain planet pairs near higher-order resonances, including Kepler-29 bc: 9:7 (Fabrycky et al. 2012; Migaszewski et al. 2017), TOI-178 bc: 5:3 (Leleu et al. 2021), TOI-1136 ef: 7:5 (Dai et al. 2023), Kepler-138 cde: 5:3-5:3 (Jontof-Hutter et al. 2015), and TRAPPIST-1 bcd: 8:5-5:3 (Gillon et al. 2017; Huang & Ormel 2022). Higher-order resonances are known for some Solar System objects (Murray & Dermott 1999), such as those between Neptune and many Kuiper Belt Objects (e.g. Volk & Malhotra 2025; Smirnov 2025; Chiang et al. 2003) although there is a striking deficit of them in the asteroid belt (DeMeo & Carry 2013).

These observations prompted us to investigate the formation of higher-order MMR in Kepler-like systems through Type-I disk migration. While previous works (Xiang-Gruess & Papaloizou 2015; Xu & Lai 2017) studied capture into second-order resonance of isolated pairs of planets, we investigated both second-order and third-order resonances in systems with more than two planets. We also incorporated a disk inner edge in our migration

simulations based on the truncation of the disk at the magnetospheric boundary (Masset et al. 2006; Izidoro et al. 2017; Wong & Lee 2024), which is crucial for stopping the migration before the planets fall onto the star and for converting divergent encounters into convergent ones. Moreover, our simulations included protoplanetary disks of surface densities as low as 10 g cm^{-2} at 1 AU (two orders of magnitude smaller than the Minimum Mass Solar Nebula, MMSN, Hayashi 1981) to mimic transitional disks or truncated disks, which may be relevant to small planet formation (Choksi & Chiang 2020; Lee & Chiang 2016).

In Section 2, we describe our numerical model for disk migration. In Section 3, we present two case studies of how higher-order MMR are produced during Type-I migration. We discuss population-level results in Sections 4. Finally, Section 5 contains a brief summary of this paper.

2. METHODS

2.1. *Disk Migration Setup*

We focus on Type-I migration of low-mass planets that do not carve a gap in protoplanetary disks (see Kley & Nelson 2012, and references therein). Specifically, we investigate the stage of disk migration after planets have grown to their final masses (post-disk, mass loss and mergers may still be possible but are not simulated here). See also the alternative approach by e.g. Izidoro et al. (2017) who grow the planets while migrating them. One benefit of our methodology is that we have better control of the final orbital architecture: stellar mass, planet mass, intra-system uniformity, etc. As will be described shortly, we strive to reproduce the observed Kepler-like planets.

Type-I migration torque depends on local disk conditions, including the surface density Σ and the disk aspect ratio $h \equiv H/R$. To simplify our model, both were assumed to be power laws:

$$\Sigma = \Sigma_{1\text{AU}} \left(\frac{r}{1AU} \right)^{-\alpha} \tag{1}$$

$$h = h_{1\text{AU}} \left(\frac{r}{1AU} \right)^{\beta} \tag{2}$$

where $\Sigma_{1\text{AU}}$ and $h_{1\text{AU}}$ are the surface density and the aspect ratio at 1 AU and r is the radial distance from the host. α and β are the power-law indices. In this work, we set α to 1.5 following the MMSN (Hayashi 1981), and the disk flaring index β to 0 i.e. no flaring. We drew $\Sigma_{1\text{AU}}$ from a log-uniform distribution between 10 and 10,000 g cm^{-2}. We adopt a wide range for the surface density to encompass the MMSN (~ 1700 g cm^{-2} Hayashi 1981) as well the Minimum-Mass Extrasolar
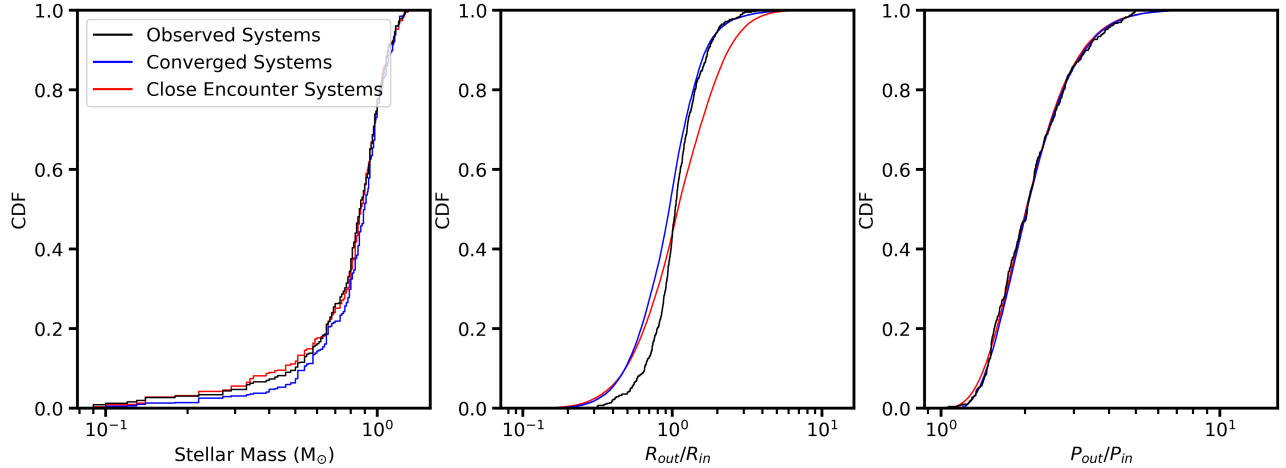
Figure 1. Cumulative distribution functions (CDFs) of stellar mass, radius ratio and period ratio between neighboring planets. The black curves show the 239 confirmed multi-planet ($N_p \geq 3$) systems from the NASA Exoplanet Archive. In blue and red, we display the corresponding values from our simulations. Note that the period ratios are initial period ratios. The red curves denote systems that experienced some close encounters and are hence discarded (see Section 2.4). The blue curves represent the systems that completed disk migration.

Nebula which is estimated to be a factor of few denser than MMSN (Chiang & Laughlin 2013; Dai et al. 2020; He & Ford 2022). Additionally, sub-Neptune formation may occur in transitional disks (Lee & Chiang 2016) or in truncated disks (Dupuy et al. 2016), both of which may have significantly depleted surface densities.

Our prescription for migration timescales follows Pichierri et al. (2018) and references therein. τ_a (Eqn. 3) is the decay timescale for the semi-major axis, and τ_e (Eqn. 4) is the timescale for eccentricity damping by the disk. The ratio of τ_a to τ_e is the K-factor (Eqn. 5):

$$\tau_a \simeq \frac{1}{2.7 + 1.1\alpha} \frac{M_*}{m} \frac{M_*}{\Sigma a^2} \frac{h^2}{\sqrt{GM_*/a^3}} \tag{3}$$

$$\tau_e \simeq \frac{1}{0.780} \frac{M_*}{m} \frac{M_*}{\Sigma a^2} \frac{h^4}{\sqrt{GM_*/a^3}} \tag{4}$$

$$K = \frac{\tau_a}{\tau_e} \simeq \frac{0.780}{2.7 + 1.1\alpha} h^{-2} \tag{5}$$

where M_* is the stellar mass, m is the planet mass, and a is the planet's semi-major axis. We drew K from a log-uniform distribution between 10 and 1000. The aspect ratio h is derived by inverting Eqn. 5 and is generally between 0.01-0.1.

To prevent the planets from falling onto the host star, we introduced an inner disk edge where the migration torque is reversed (Masset et al. 2006; Izidoro et al. 2017; Wong & Lee 2024). Resonant capture occurs only during convergent migration (where period ratio decreases, see e.g. Batygin & Morbidelli 2013). The inner disk edge further facilitates the formation of resonant chains

by converting divergent encounters into convergent ones, allowing longer-period planets to catch up with the planets that have already reached and stopped at the inner disk. We fixed the inner disk edge at 0.05 AU, with a width of 0.01 AU to represent the location of magnetospheric truncation where the magnetic forces from the host star disrupt the accretion flow (e.g. Shapiro & Teukolsky 1983). Following the suggestion of Batygin et al. (2023) that the period associated with a test particle at the inner disk edge depends weakly on host star masses, we used the same inner disk edge in our simulations.

All of these disk migration prescriptions were implemented with the `type_I_migration` (Kajtazi et al. 2023) scheme in `REBOUNDx` (Tamayo et al. 2020) and `REBOUND` (Rein & Liu 2012). We used the symplectic `WHFAST` integrator (Wisdom & Holman 1991; Rein & Tamayo 2015). The time step was set to 1/20 of the Keplerian orbit at the inner disk edge. This method relies on N-Body simulations with prescriptions for Type-I migration developed to match the results of hydrodynamic simulations, not the hydrodynamic simulations themselves. Several studies have characterized the formation of MMRs in hydrodynamic simulations directly (Cresswell & Nelson 2008; Cresswell & Nelson 2008; Ataiee & Kley 2021a; McNally et al. 2019).

Our systems were generally evolved for $3\tau_a$. Protoplanetary disk lifetime depends on stellar mass (Ribas et al. 2015), with some disks around low mass stars lasting 20 Myr or longer (Long et al. 2025; Silverberg et al. 2020). Disks around stars up to $2M_\odot$ may survive up to 15 Myr (Wilhelm & Portegies Zwart 2022), though

typical disk lifetimes are ~ 3 Myr (Haisch Jr et al. 2001; Li & Xiao 2016). Based on these disk dispersal constraints, we set an upper limit on the integration time of 10 Myr. We also set a minimum integration time of 30 kyr if $3\tau_a < 30$ kyr.

2.2. *Mimicking Observed Kepler-like Systems*

In our simulations, we strive to match the stellar masses, planetary radii/masses, orbital period ratios, and multiplicity, and intra-system uniformity observed in confirmed exoplanetary systems. We downloaded the confirmed planets from NASA Exoplanet Archive [1] on August first 2024, focusing on systems with at least three transiting planets. We excluded planets that are likely too massive for Type-I migration ($> 30M_\oplus$). This resulted in a total of 239 confirmed multi-planet systems with up to seven planets.
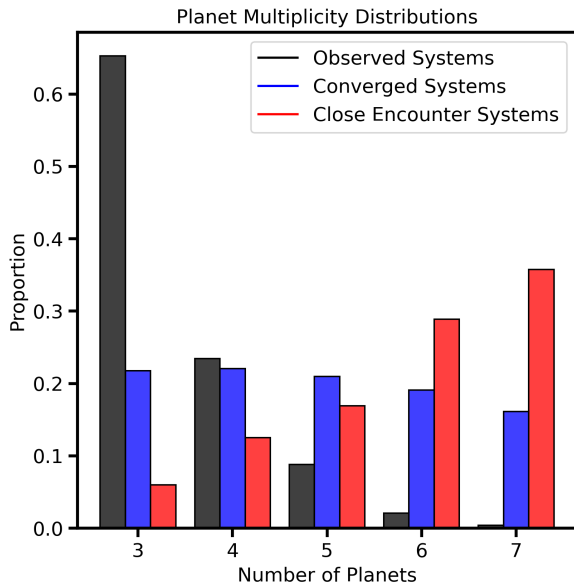
Figure 2. Planet multiplicities for observed systems (black), systems that experienced close encounters (red), and systems that complete disk migration with no close encounters (blue). Note that observed multiplicity is smaller than the actual multiplicity. Section 2.4 explains why close encounters are more common in higher-multiplicity systems. The blue systems were used in our subsequent analysis.

To simulate a planetary system, we first drew a sample from the confirmed planetary systems. We adopted the reported stellar mass. We directly used the observed radii of the observed planets at the observed ordering in

terms of semi-major axis. The innermost planet was initialized at 0.1 AU i.e. substantially far away from the inner disk edge of 0.05AU. Again, we aimed to simulate the final assembly of a resonant chain just before the planets reach the disk inner edge. The initial orbital periods of longer-period planets were set to be non-resonant. Specifically, we put down additional planets by drawing orbital period ratios from a natural log-space fit (16th percentile: 1.54, 50th percentile: 2.03, 84th percentile: 2.88) of the observed period ratio distribution between neighboring planets (e.g. Fabrycky et al. 2014; Weiss et al. 2018). The vast majority of neighboring planets had initial period ratios between 1.2-5 (see Fig. 1).

The actual multiplicity of a confirmed planetary system is probably higher than the observed multiplicity (see e.g. Zhu & Dong 2021; Turtelboom et al. 2024). As the observed sample is dominated by three planet systems, we generated more four to seven planet systems until all multiplicities had roughly the same number of systems (Fig. 2). We add more planets by repeatedly drawing from the same logarithmic distribution of period ratios as we described above. Moreover, to capture the intra-system uniformity in planet size ('peas-in-a-pod' pattern Weiss et al. 2018; Wang 2017; Millholland et al. 2017a), we also fitted a distribution of radius ratios between neighboring planets in natural log space (16th percentile: 0.708, 50th percentile: 1.06, 84th percentile: 1.57). Each new planet has a radii that depends on the radii of the planet directly interior to it and a random sample from this log-normal distribution.

Planet masses were determined from the radii and the mass-radius relationship `Forecaster` (Chen & Kipping 2017). In essence, this is a power law: $R = M^{0.279}$ for $M < 2M_\oplus$ and $R = M^{0.59}$ for $M > 2M_\oplus$) with intrinsic scatter. Sometimes, `Forecaster` can produce masses that are perhaps so large that Type-I migration is not an accurate description. If we drew a mass $> 30M_\oplus$, we simply drew again.

In Figures 1 and 2, we compare our simulated systems with observation. Our simulated sample emulates the observed sample in terms of stellar mass and neighboring planet radius and period ratios. In other words, our simulated planetary systems retain the previously reported stellar-mass-planet-size correlation (e.g. Wu 2019) and the 'peas-in-a-pod' pattern (Weiss et al. 2018; Wang 2017; Millholland et al. 2017b).

Although some studies have prescribed nonzero initial eccentricity and inclinations (e.g. Izidoro et al. 2017), we set the initial eccentricity and orbital inclination of each planet to zero since we expect disk damping prior to resonant encounters. The mean anomaly was drawn from uniform distributions between 0 and $360°$.
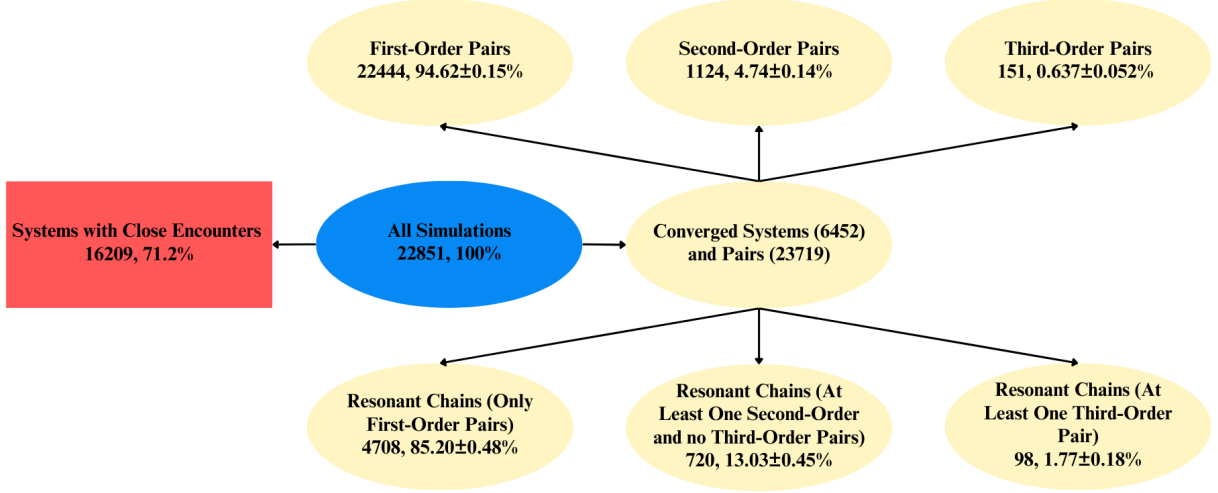
Figure 3. More than 70% of our simulations were discarded due to having close encounters. Among the remaining systems: $\sim 5\%$ and $\sim 0.5\%$ of resonant planet pairs were in librating second- or third-order resonances; $\sim 13\%$ and $\sim 1\%$ of planetary systems classified as three-body resonant chains and two-body resonant chains contain at least one second-order or third-order resonance.

2.3. *Identifying Mean-Motion Resonance*

In the literature, Δ is frequently used as a convenient metric to identify MMR:

$$\Delta \equiv \frac{P_c/P_b}{p/q} - 1 \qquad (6)$$

for a pair of planets bc near the integer ratio $p\colon q$. When the dynamical state of a planetary system is unknown, measuring $\Delta \simeq 0$ quickly identifies near-resonant planets (e.g. Huang & Ormel 2023; Dai et al. 2024). However, the hallmark of true resonance is the libration of a resonant angle in the presence of a separatrix, a generalized coordinate for the resonant Hamiltonian (Murray & Dermott 1999). The two-body resonant angle, ϕ_{bc}, between planets b and c is given by:

$$\phi_{\mathrm{bc}} = q\lambda_b - p\lambda_c + (p - q)\hat{\varpi}_{bc} \qquad (7)$$

where λ are the planets' mean longitudes and $\hat{\varpi}_{bc}$ is the mixed longitude of the pericenter (Sessin & Ferraz-Mello 1984; Henrard et al. 1986; Wisdom 1986; Batygin & Morbidelli 2013). Hadden (2019b) demonstrated that $\hat{\varpi}_{bc}$ is an acceptable approximation for higher-order:

$$\hat{\varpi}_{bc} = \arctan\left(\frac{fe_b \sin \varpi_b + ge_c \sin \varpi_c}{fe_b \cos \varpi_b + ge_c \cos \varpi_c}\right) \qquad (8)$$

where e_b and e_c are the eccentricities of each planet and f and g are coefficients from the expansion of the disturbing function.

For a pair of planets in MMR, ϕ_{bc} librates (oscillates with a bounded amplitude) around an equilibrium point rather than circulating between 0° to 360°. We estimate the libration amplitude following Millholland et al. (2018):

$$A = \sqrt{\frac{2}{N} \sum (\phi - \langle\phi\rangle)^2} \qquad (9)$$

where N is the number of snapshots, ϕ is the resonant angle, and $\langle\phi\rangle$ is the mean resonant angle over the N samples (a proxy for the equilibrium point). We identify MMR as pairs of planets with libration amplitude $A < 90°$ at the end of our disk migration simulation.

A triplet of planets can also be engaged in zeroth-order three-body, Laplace-like MMR e.g. the TRAPPIST-1 planets (Agol et al. 2021) or our Galilean moons (Peale 1976). For planets b, c, and d, the ϕ_{bcd} is defined by Eqn. 10.

$$\phi_{bcd} = \phi_{bc} - \phi_{cd} = q_{bc}\lambda_b - (p_{bc} + q_{cd})\lambda_c + p_{cd}\lambda_d \quad (10)$$

where p and q are the integers of two-body MMR for the b-c pair and c-d pair. The above expression applies
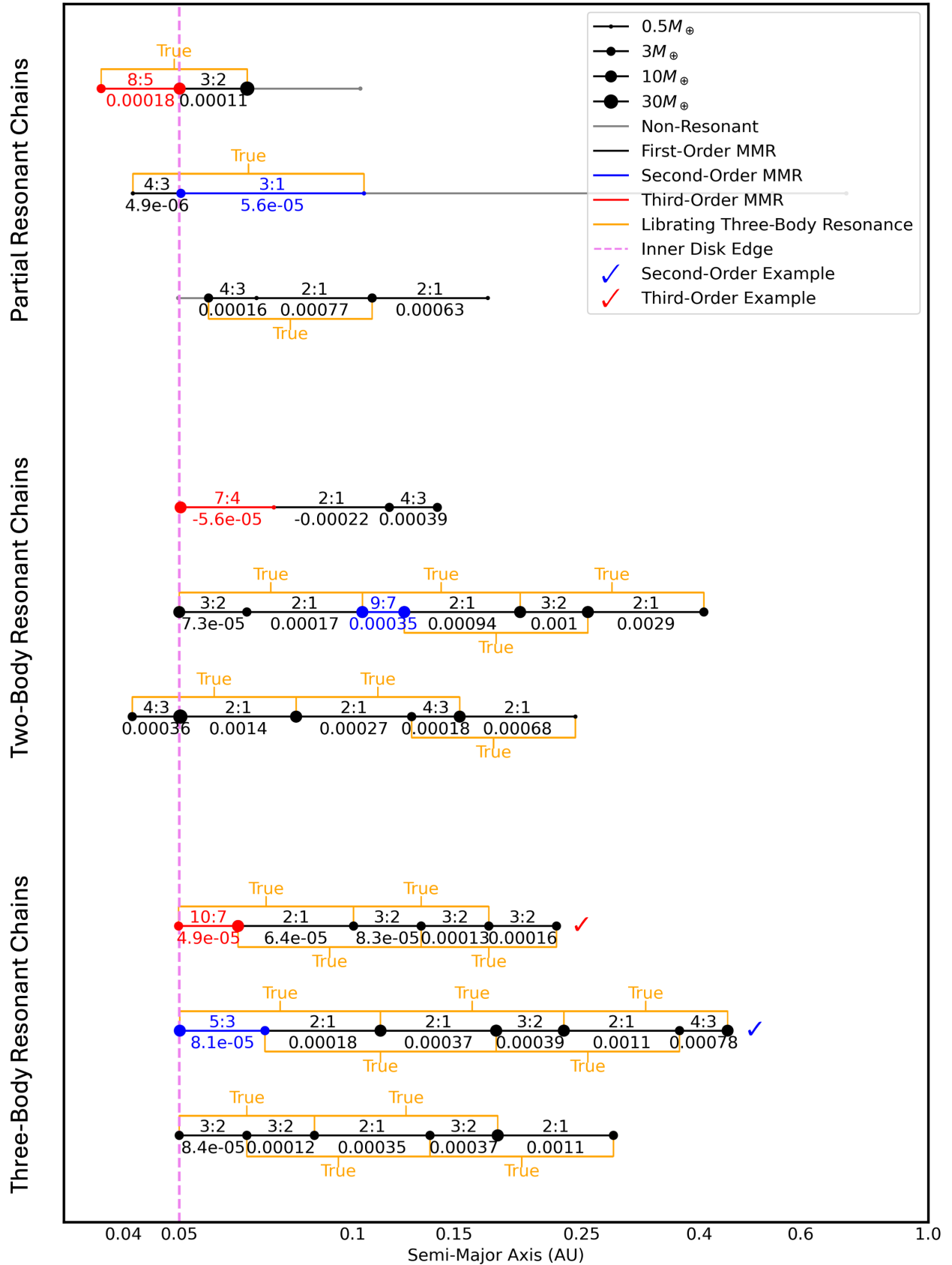
Figure 4. A representative set of nine systems at the end of our simulations. We label each resonant pair of planets with its integer ratio and deviation Δ. Colors indicate the order of resonance: nonresonant in grey, first-order in black, second-order in blue, and third-order in red. Librating three-body resonant angles are shown in orange. Two case study systems in Section 3 are indicated with check marks. The top three systems are 'Partial Resonant Chains' (at least one pair not in MMR); the middle three are 'Two-Body Resonant Chains'; the bottom three are 'Three-Body Resonant Chains.'

when the constituent two-body MMRs are both of the same order. If two different order two-body resonances are involved ($|p_{bc} - q_{bc}| \neq |p_{cd} - q_{cd}|$), the expression is modified by multiplying each two-body angle by order of the other pair to eliminate any dependence on ϖ. For three body resonance angles, we use the standard longitude of the pericenter ϖ_c instead of the mixed longitudes $\hat{\varpi}_{bc}$ or $\hat{\varpi}_{cd}$. Siegel & Fabrycky (2021) noted that the libration of three-body MMR prefers a center of $180°$. We again identify three-body MMR as triplets with libration amplitude $A < 90°$. At the end of disk migration simulations, we examined the prevalence of both two-body and three-body MMR.

If there are more than two or three planets in a resonant arrangement in a system, we can prescribe an N-body resonant angle where N is the number of planets in the arrangement. However, these are very difficult to constrain even in systems that are deeply in resonance like TOI-1136 (Dai et al. 2023). Instead, it is appropriate to define a "resonant chain" where all planets pairs and/or triplets in the system have librating two- and/or three-body resonant angles. We adopt the following terms to describe resonant chains (see also examples in Fig. 4):

1. Complete Three-Body Resonant Chain: All neighboring triplets of planets exhibit librating three-body resonant angles and all neighboring pairs have librating two-body resonant angles.

2. Complete Two-Body Resonant Chain: All neighboring pairs exhibit librating two-body resonant angles and only some (or none) of the triplets have librating three-body resonant angles.

3. Partial Resonant Chain: Some planet pairs exhibit librating two-body resonant angles while others are non-resonant. Any number of triplets may have librating three-body resonant angles.

In all cases, the two-body MMRs can be of any order. We examined all 36 first-, second-, and third-order MMRs ranging from period ratio of 1.1 (11 : 10) to 4 (4 : 1). This range encompasses the smallest observed pairwise period ratios (Kepler-36bc 7:6, see Carter et al. 2012) to the widest third-order resonance, 4:1. We compiled a library of corresponding f and g coefficients for each p and q using the `disturbing_function.get_fg_coefficients` routine from `celmech` (Hadden & Tamayo 2022).

2.4. *Handling Close Encounters*

We ran a total of $22,851$ simulations, roughly $\sim 70\%$ of which experienced close encounters. Since symplectic integrators are not designed to handle close encounters (Wisdom & Holman 1991), we stopped and discarded any simulations where planets ventured within five mutual Hill radii of each other, following Weiss et al. (2018) who noted that Kepler systems tend to have significant spacings between planets. We note that close encounters do not necessarily prevent a system from developing a resonant chain eventually (Izidoro et al. 2017). However, our simulation setup is currently not equipped to accurately predict the outcome of close encounters. We defer that to a future work as we are more concerned with determining the orders of MMRs that form during disk migration than running comprehensive population synthesis and planet growth calculations.

As evident in Fig. 2 and 10, systems with close encounters generally feature higher planet multiplicity, more massive outer planets, and faster migration than the systems that quiescently completed disk migration. Close encounters are known to be more common in high multiplicity systems (Smith & Lissauer 2009) and it has been suggested that longer resonant chains are less stable as they tend to experience a secondary resonance between a libration frequency and a fraction of the synodic frequency (Matsumoto et al. 2012; Pichierri & Morbidelli 2020; Goldberg et al. 2022). A more massive outer planet also makes resonances less stable and more prone to disruption (e.g. Goldreich & Schlichting 2014; Deck & Batygin 2015; Xu & Lai 2017). Finally, faster migration makes it less likely for planets to capture into resonance (Batygin & Morbidelli 2013). The fact that we initialized systems with zero mutual inclination may have further increased close encounters.

3. CASE STUDIES OF SYSTEMS THAT DEVELOPED HIGHER-ORDER RESONANCE

Both second- and third-order MMR emerged in our disk migration simulations. Before we present population-level results (Section 4), let's examine the migration history (Fig. 6) of a particular system that ended up with a 5:3 second-order resonance. The system's architecture is shown in Fig. 4 (eighth row), and its initial conditions are presented in Tab. 2.

In this particular system, seven planets were initialized between 0.1 and 1.37 AU around a $0.89M_\odot$ host star in a disk with an aspect ratio of 0.0395 and a low surface density of 16.6 g/cm^2.

The innermost two planets are the pair that eventually captured into a second-order 5:3 MMR. We denote these two planets 0 and 1 and highlight them in red in Fig. 6. Planet 0 is more massive than planet 1: $8.0M_\oplus$ v.s. $4.8M_\oplus$. Therefore, planet 0 initially migrated faster
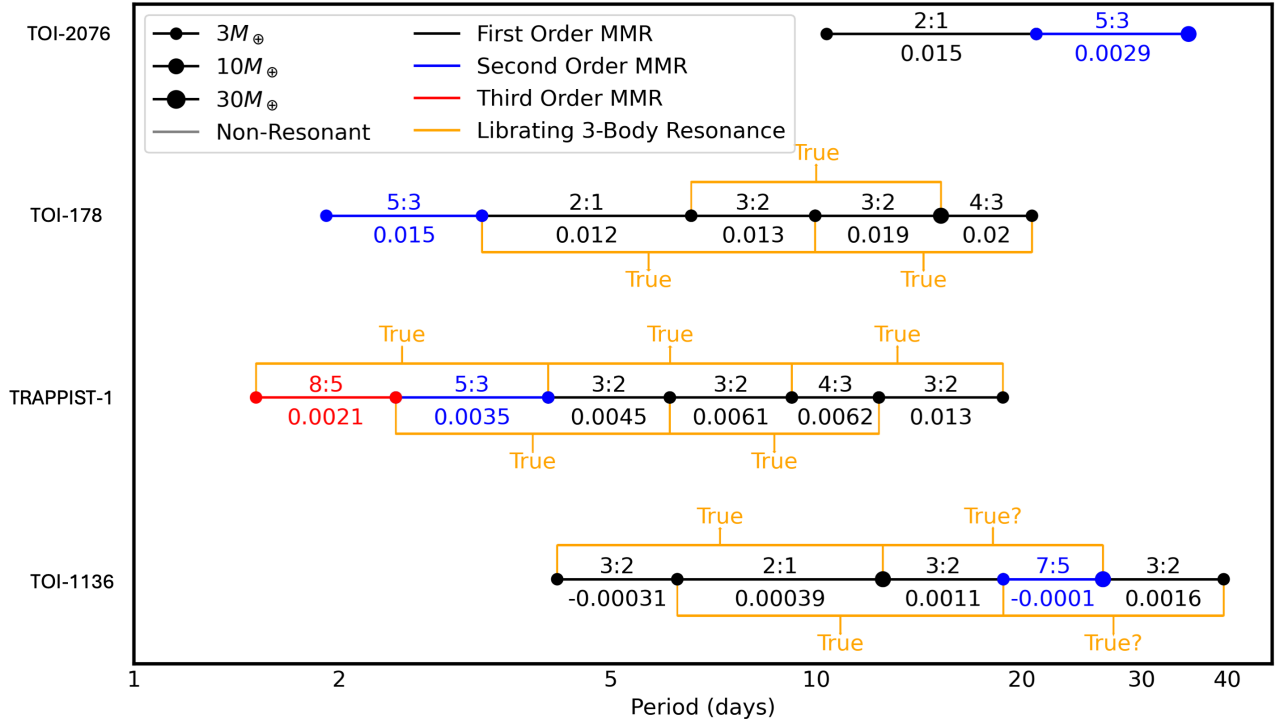
Figure 5. A subset of observed resonant chains plotted like the simulated systems shown in Fig. 4. Unlike Fig. 4, these observed systems are displayed with respect to period to reduce whitespace. In most example observed systems, it is unclear if the two-body resonant angles librate. We choose to mark the most proximal MMRs. Librating triplets are indicated in accordance with observation.

than planet 1 i.e. two planets initially experienced divergent migration.

A key milestone of their evolution is marked (1) in Fig. 6. When planet 0 reached the inner disk edge (around 50 kyr), its migration is effectively stopped, allowing planet 1 to catch up. This highlights how the inner disk edge converts divergent migration to convergent migration.

At milestone (2) or 160 kyr, planets 0 and 1 captured into a 2:1 MMR. They remained in this resonance until milestone (3) near 1010 kyr. In the intervening time 160-1010 kyr, longer period planets successively arrived at the inner edge and formed a chain of first-order resonances from planet 0 to 4.

At milestone (3), planets 5 and 6 joined the inner resonant chain of planets 0-4. It appears that as planets 5 and 6 tried to join the resonant chain, a wave of perturbations were sent through the existing chain. As a result, the innermost pair 01 left the 2:1 MMR as their periods continued to decrease.

Before reaching the next first-order MMR, 3:2, the innermost pair 01 captured into the second-order MMR 5:3 at milestone (4) around 1030 kyr. Thanks to the original 2:1 MMR, planet 0 and 1 had low but non-zero orbital eccentricity of order 0.01 before encountering the 5:3 resonance. The non-zero eccentricity was critical

for strengthening the second-order resonant interaction ($e^{|p-q|}$ and facilitated the capture, see Sections 4.1 and 4.6) for more discussion.

At milestone (5) or 1080 kyr, all seven planets fully captured into a resonant chain, all constituent two-body and three-body resonant angles entered a state of libration through to the end of the simulation.

The successful formation of a second-order resonance in this system is owed to several fortuitous factors:

- The low surface density at 1 AU of 16.6 g/cm^2 ($525 g/cm^2$ at 0.1AU) resulted in a slow migration rate.

- The longer-period planets in this seven-planet system eventually pushed the innermost pair out of the initial 2:1 resonance.

- 5:3 is the first strong resonance encountered after the innermost pair left 2:1 resonance before they can reach the next first-order 3:2.

- Due to the initial 2:1 resonance, the innermost pair of planets already had low but nonzero eccentricity before they encountered 5:3 MMR. The eccentricity might have amplified the second-order resonance.
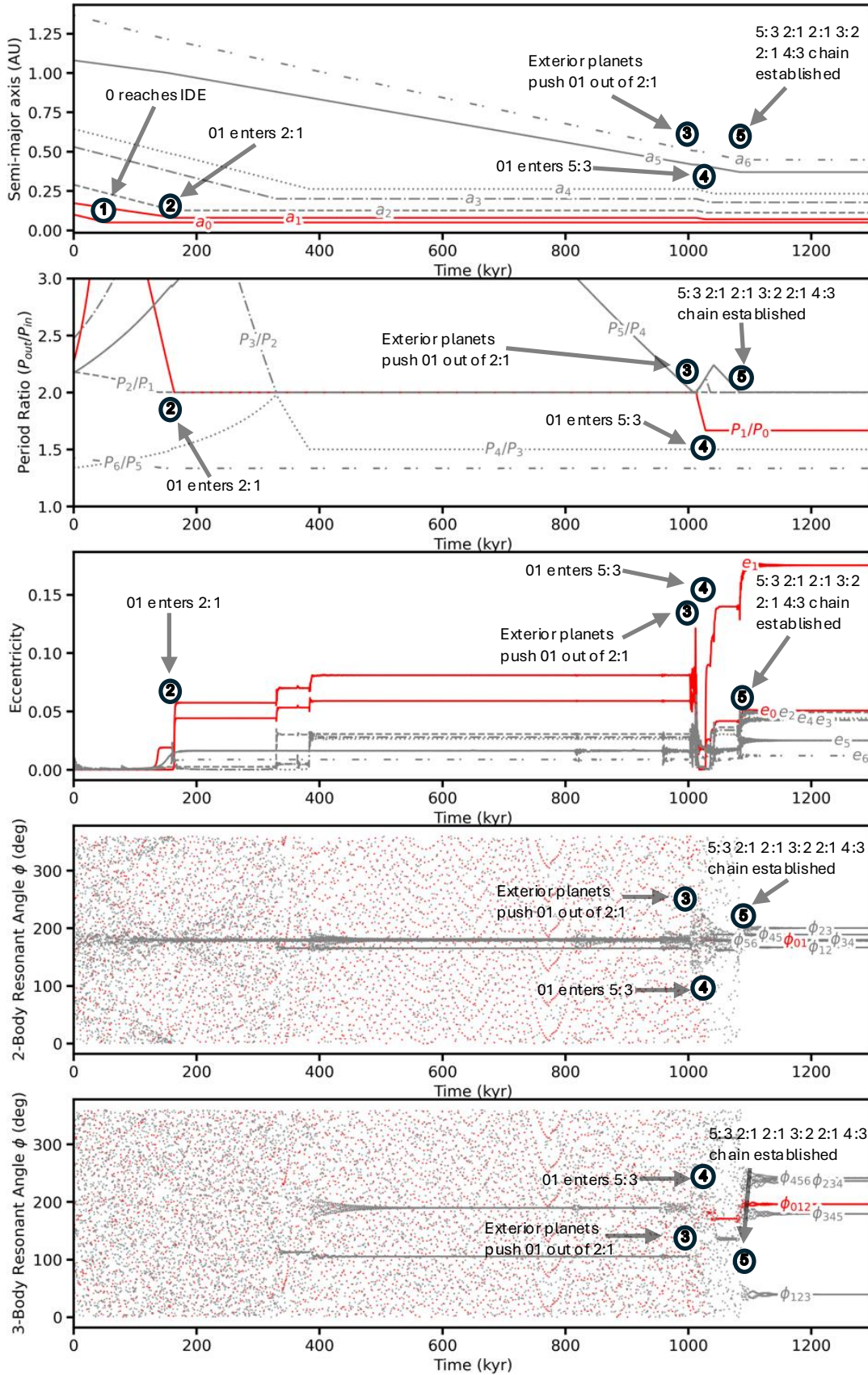
Figure 6. The migration history of a resonant chain with a second-order resonance (innermost two planets 0 and 1, shown in red). Planet 0 and 1 were initially captured into a 2:1 resonance. However, as longer-period planets joined the resonant chain, the 2:1 resonance broke and the planets captured into the nearby 5:3 resonance. A few key milestones of the evolution have been labeled. See Section 3 for a detailed description of this system. Tab. 2 contains the system parameters.

Are these conditions difficult to achieve in a typical Type-I migration simulations? We discuss that in the next section. In the Appendix, we also show the formation of a third-order 10:7 resonance in Tab. 3 and Fig. 15. Its final orbital architecture is also displayed in Fig. 4. Very briefly, this is a six-planet system around a 1.0 $M_\odot$ host star. The surface density is close to the MMSN at 2080 g/cm². The aspect ratio is 0.0991. The story is very similar to the one described above, a pair of planets were initially engaged in a 3:2 first-order MMR. However, upon breaking this resonance, the pair captured into the closest third-order resonance 10:7 before encountering any second- or first-order resonances. The initial first-order MMR may be important for setting up the capture into third-order MMR because the first-order MMR produced a small but non-zero eccentricity (see Fig. 15).

4. POPULATION-LEVEL RESULTS

On a population level, we found that Type-I disk migration coupled with an inner disk edge can produce higher-order MMRs. While this qualitative result holds, we caution that the quantitative interpretations presented in this section depend strongly on our model assumptions. Most importantly, the assumed range of disk surface densities sets the overall migration rate, which influences the fraction of different orders of MMR.

4.1. *Higher-Order Two-Body MMR Do Not Need to Form in a Three-Body Resonance*

It has been suggested in the literature that higher-order two-body resonance may form through the help of an existing three-body Laplace-like resonance. Huang & Ormel (2022) postulated that the inner three planets of the TRAPPIST-1 bcd could have initially formed in a three-body Laplace-like resonance comprised of two first-order two-body resonances, 3:2-3:2. Subsequent orbit expansion, through the help of the disk inner edge (see Section 4.8), may have allowed the system to smoothly drift to a 8:5-5:3 configuration while maintaining the libration of the same three-body resonant angle $\phi_{bcd} = 2\lambda_b - 5\lambda_c + 3\lambda_d$. It is worth noting again that 8:5-5:3 and 3:2-3:2 have the same three-body resonant angle. Kepler-221 bce may be another triplet of planets that have evolved while preserving a three-body Laplace resonance (Goldberg & Batygin 2021; Yi et al. 2025).

During this expansion of a three-body Laplace resonance, the period ratios of three planets—labeled 0, 1, and 2 (with 0 being the innermost and 2 the outermost)—involved should satisfy this relation so as to maintain the libration of the three-body resonant angle (Rath et al. 2022):

$$\frac{P_2}{P_1} = \frac{p_{12}}{p_{01} + q_{12} - q_{01}(P_0/P_1)^{-1}} \qquad (11)$$

in a P_0/P_1-P_2/P_1 plot (Fig. 7). If a particular three-body Laplace resonance is preserved, a system would evolve along the dashed curves.

However, in our simulations, higher-order MMRs do not evolve along three-body resonance tracks (dashed lines in Fig. 7). Let's examine again the two case studies presented in Section 3. The actual migration histories of these two systems are horizontal or vertical i.e. the planets interact under the influence of two-body resonances. In other words, the systems captured into second- and third-order two-body resonances without first establishing a three-body Laplace-like resonance.

We stress that roughly 79% of the higher-order resonances in our simulations eventually become part of a librating three-body Laplace resonance with its neighboring planets. However, these three-body Laplace resonances were established as a result of the two-body resonances rather than the other way around (see Fig. 6 and Fig. 8). 21% of our higher-order resonances are not engaged in three-body resonances with neighboring planets at the end of the simulations. Our findings suggest that two-body higher-order MMR can form without the help of a three-body Laplace-like resonance. We suspect that direct capture into two-body higher-order MMR does not apply to TRAPPIST-1 bcd because Agol et al. (2021) showed the three-body Laplace angle between bcd librates, while the two-body resonant angles circulate in most of the posterior samples. Even in the small fraction where two-body resonant angles librate, TRAPPIST-1 bc and cd librate around 3:2-3:2 rather than the observed 8:5-5:3 resonances (Agol, private comms). In other words, 8:5-5:3 resonances were unlikely to be produced by direct capture into two-body higher-order resonances. On the other hand, direct capture into two-body higher-order MMR is the natural explanation for TOI-1136 ef where the two-body angle is likely librating (Dai et al. 2023).

4.2. *Eccentricity Excitation Caused by Pre-Existing First-Order MMR Promotes Higher-Order Capture*

In our simulations, we observe that most higher-order MMR pairs were formed after the system encounters and escapes from a previous first-order MMR. As second-order is the dominant population of these higher-order pairs, we focus on that configuration in this subsection. We argue that the eccentricity excitation by the previous first-order MMR promotes the subsequent capture into a second-order MMR.
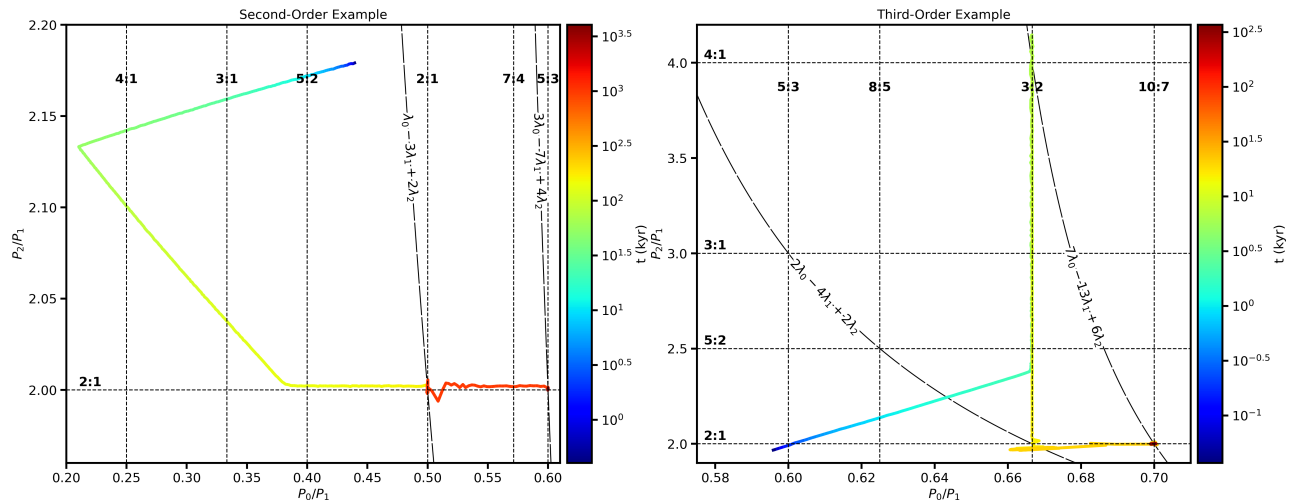
Figure 7. The period ratio evolution of a triplet of planets that end up in higher-order MMR (case study systems presented in Section 3). The color coding indicates the time since the start of the simulation. Horizontal and vertical straight lines indicate two-body resonance between the inner and outer pair of planets. Dashed curves by Eqn. 11 show the evolution track if a librating three-body Laplace-like resonance is preserved. In both systems, the planets evolved horizontally i.e. they captured into 5:3 and 10:7 resonance directly without forming a three-body resonance first.

MMR capture is eccentricity dependent; in the limit of adiabatic evolution (infinitely slow migration), capture is certain at small initial eccentricity, and becomes probabilistic once the eccentricity exceeds $\sim \mu^{1/3}$ for first-order MMR and $\sim \mu^{1/2}$ for second-order MMR (Batygin 2015; Xu & Lai 2017), where μ is the planet-star mass ratio. As a result, the claim in Section 3 that previous eccentricity excitation promotes capture may sound counterintuitive. However, once we consider the finite rate of migration, there is a separate effect that strongly suppresses higher-order MMR capture for small initial eccentricity. This effect originates from a key difference between first-order and higher-order ($|p-q| \geq 2$) MMRs: Since the resonant term in the Hamiltonian is of order $e^{|p-q|}$, for a higher-order resonance, the zero-eccentricity state is a fixed point of the Hamiltonian except for a finite width around the resonance (Fig. 8 bottom left panel). Therefore, an initially circular orbit will stay at approximately zero eccentricity until the system encounters the resonance. This creates a problem for resonance capture: at zero eccentricity, the strength of resonant coupling also vanishes, and the eccentricity cannot evolve fast enough to follow the stable fixed point of the Hamiltonian to become captured as it does in the adiabatic limit; instead, the system will directly pass through the resonance. The orange line in Fig. 8 bottom center panel is an example of this; Xu & Lai (2017) offers a more quantitative discussion on when capture becomes suppressed by low initial eccentricity. We note that the same problem does not occur for first-order MMR because there the eccentricity of the stable fixed

point smoothly increases as the system approaches the resonance. As a result, orbits with low initial eccentricity already acquire finite eccentricity when it encounters resonance and can be easily captured (Fig. 8 top left and top center panels).

To give a more quantitative estimate on how this mechanism affects capture, we consider a toy problem with a pair of planets where the inner planet has $\mu = 3 \times 10^{-5} \approx 10 M_\oplus/M_\odot$ and the outer planet is a test particle migrating at $\tau_a = 10^7 P_1$, $\tau_e = 10^5 P_1$. The mass scale and the migration timescales resemble typical low-mass planets near the edge of the protoplanetary disk. The result is summarized in the right panels in Fig. 8. For second-order resonance, capture is suppressed for initial eccentricity $\lesssim 10^{-3}$; meanwhile, for first-order resonance, capture is guaranteed at low eccentricity. (We also see the reduction of capture probability at high eccentricity, which occurs for both first- and second-order MMRs.) The minimum eccentricity required for capturing into a second-order MMR is already larger than what can be produced by the non-resonant interaction between low-mass planets. As a result, capturing into a higher-order resonance requires some additional eccentricity excitation, which can be provided by a previous encounter with a first-order MMR. This pathway offers a promising alternative to the Laplace-like capture described in Section 4.1.

This pathway also naturally explains the observation in Section 4.6 that higher-order MMRs show higher eccentricity. The eccentricity of a captured pair mainly depends on the ratio between eccentricity damping and
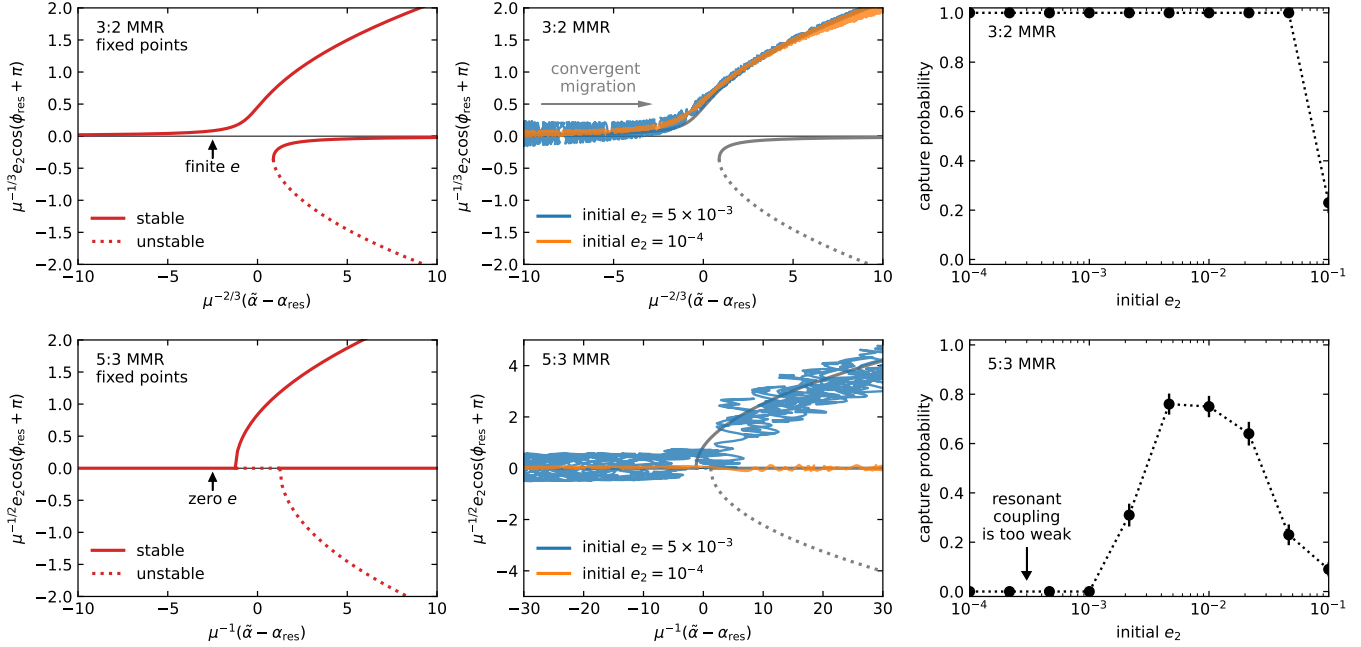
Figure 8. A comparison between capturing into first-order and second-order MMR. For simplicity, we consider a restricted three-body problem where the outer planet is a test particle and the inner planet has planet-to-star mass ratio μ. Left panels: fixed points of the Hamiltonian. Compared to similar plots in the literature (e.g., Fig. 1 in Batygin 2015), we opt for explicitly expressing the resonant parameter (horizontal axis) and canonical variable (vertical axis) in terms of physical quantities. The resonant parameter (horizontal axis), with $\alpha_{\rm res} = (q/p)^{2/3}$ and $\tilde{\alpha} = (a_1/a_2)(1+\frac{p}{p-q}e_2^2)$, is conserved in the absence of migration. For first-order MMR, the eccentricity of the fixed point smoothly increases as the system approaches resonance. However, for second-order MMR, the fixed point stays at $e = 0$ until encountering resonance. Center panels: simulations at different initial eccentricities. In all runs, we initialize the pair at 2% away from the resonance, and evolve the massless outer planet with $\tau_{\rm a} = 10^7 P_1$, $\tau_{\rm e} = 10^5 P_1$. For a second-order MMR, low initial eccentricity causes insufficient coupling at resonance, and the system cannot become captured by following the stable fixed point with finite eccentricity. Right panels: capture probability for the toy problem as a function of initial eccentricity. Each point is estimated using 100 simulations starting at random phases. Second-order MMR differs from first-order MMR in that low eccentricity can prevent capture (Xu & Lai 2017). As a result, eccentricity excitation from a previous first-order MMR capture generally promotes capturing into a higher-order MMR.

migration, with $e \sim \sqrt{\tau_e/\tau_m}$. To capture a pair into a higher-order MMR through the above pathway, a sufficiently high τ_e/τ_m is necessary because otherwise the eccentricity inherited from the previous resonance would have been exponentially damped while the pair migrates between resonances.

4.3. *The Prevalence of Higher-Order MMRs*

At the end of our simulations, we produced a total of 22,444 pairs of planets in first-order MMRs, 1124 in second-order MMRs, and 151 in third-order MMRs (Fig. 3). Second- and third-order MMRs correspond to $4.74 \pm 0.13\%$ and $0.637 \pm 0.052\%$ of the produced MMRs. If, instead, we count the number of planetary systems that contain at least one higher-order MMR, we found that $720/5494$ or $13.03 \pm 0.45\%$ contain at least one second-order resonance, $98/5494$ or $1.77 \pm 0.18\%$ contain at least one third-order resonance.

Focusing on systems where some planets are not incorporated in a resonant chain (labeled 'Partial Resonant

Chains' in Section 2.3), second- and third-order resonances occur at higher rates: $20.0 \pm 1.3\%$ and $2.6 \pm 0.5\%$ respectively. This difference is because the migration rate is generally slower in Partial Resonant Chains as some planets have not reached the inner disk yet. As demonstrated in Section 4.4, higher-order MMRs prefer slower migration.

As we cautiously noted above, these fractions of higher-order resonance critically depend on the prior range of disk surface density we assumed ($10 - 10,000$ g cm^{-2}, see Section 2.1). Observational constraints on the surface densities of the innermost 1AU of protoplanetary disk are lacking (e.g. Andrews 2020). The more robust results from our simulations are the relative proportion of individual resonances e.g. the fraction of planets in 5:3 v.s. 7:5 MMR.

A complete list of the two-body resonances and their relative frequencies are shown in Tab. 4 in the Appendix. In Fig. 9, we compare the frequencies of indi-
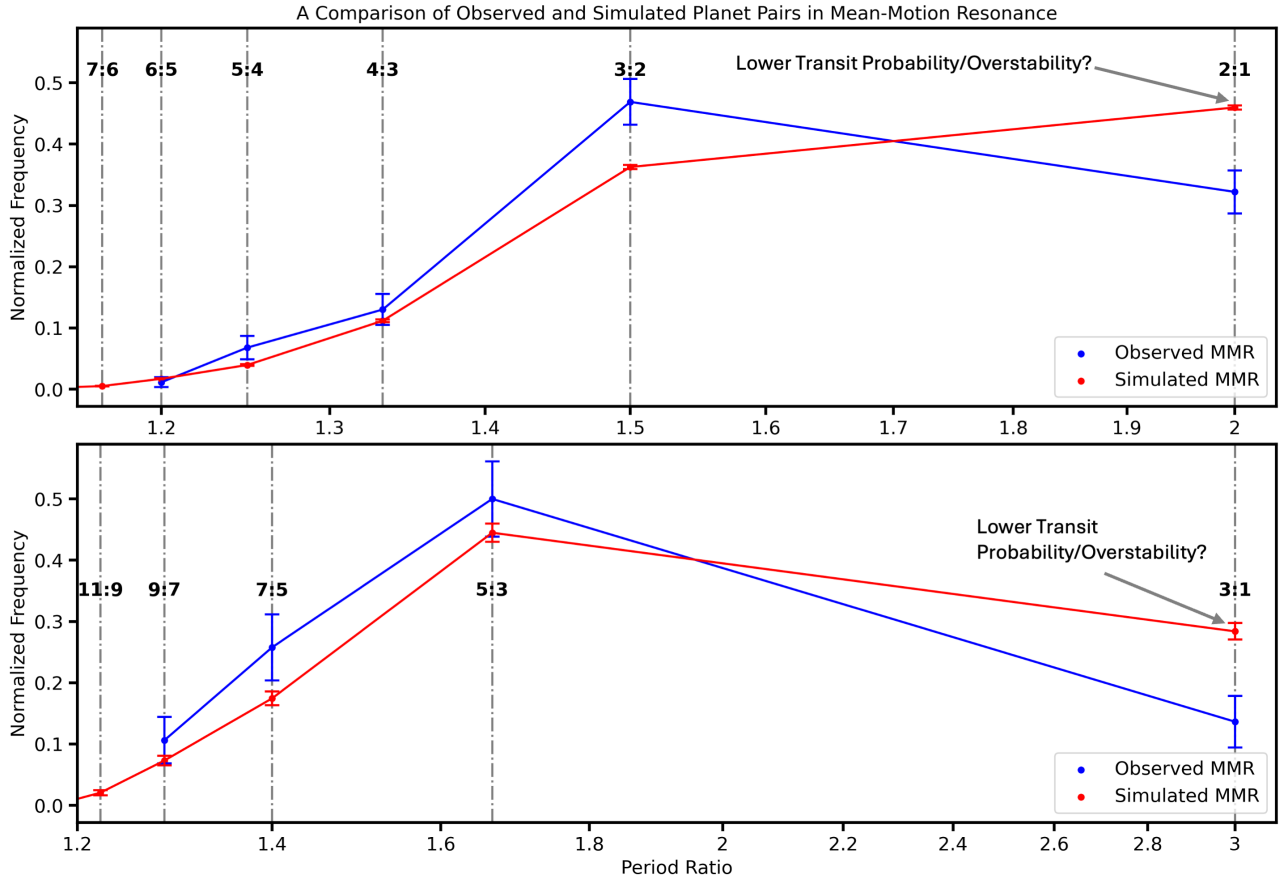
Figure 9. The relative frequencies of individual first (top panel) and second-order (bottom panel) MMR in our simulations and in the confirmed all-ages planet sample from Dai et al. (2024). Note in the simulated samples, all planet pairs have librating resonant angles. In the observed sample, there is not enough information to determine the dynamical state of the planets. Simulations produced more 2:1 and 3:1 resonance than observed. Smaller transit probabilities for inclined planets may underestimate planet counts (and thus over estimate planet separations). Alternatively, overstability may preferentially remove 2:1 and 3:1 MMRs directly (Goldreich & Schlichting 2014; Deck & Batygin 2015; Xu & Lai 2017).

vidual MMRs in our simulations with the observed sample reported in Dai et al. (2024). We find good agreement between the simulations and observations. Notably, within each order of MMR, the resonances with smaller period ratios (defined P_{out}/P_{in}) are increasingly rare, both in simulations and observations. These fractions depend on the distribution of initial period ratios, which is why we selected a wide period ratio space that mimics the Kepler sample. This is because the planets have to avoid being captured into all preceding resonances before reaching the deeper resonances (Kajtazi et al. 2023). For instance, both example systems in Section 3 capture into the resonance with the next largest period ratio after breaking from a first-order MMR. 5:3 is the most populated resonance in both simulations and observations, as this is the first strong and stable second-order resonance. Steffen & Hwang (2015) also noted 5:3

is the most prominent second-order resonance among the Kepler sample (see also Bailey et al. 2022).

Curiously, the 2 : 1 and 3 : 1 MMRs are more common in our simulations than in the observed sample. 2:1 even dominates over 3:2, which is the most prevalent observed first-order resonance. One factor that reduces the frequency of 2:1 and 3:1 MMRs is resonance overstability. Previous works (e.g. Goldreich & Schlichting 2014; Deck & Batygin 2015) pointed out that a pair of planets captured into 2:1 MMR may easily escape the resonant state upon further eccentricity damping (overstable libration). If we assume $\tau_e \propto m$, the stability criterion for first-order and second-order resonances is generally $m_1/m_2 \gtrsim 1$, but it goes as $m_1/m_2 \gtrsim 12$ for 2:1 (Deck & Batygin 2015) and $m_1/m_2 \gtrsim 8$ for 3:1 (Xu & Lai 2017).

However, this effect does not fully explain the discrepancy between our simulation and observation. Resonance overstability requires disk eccentricity damping
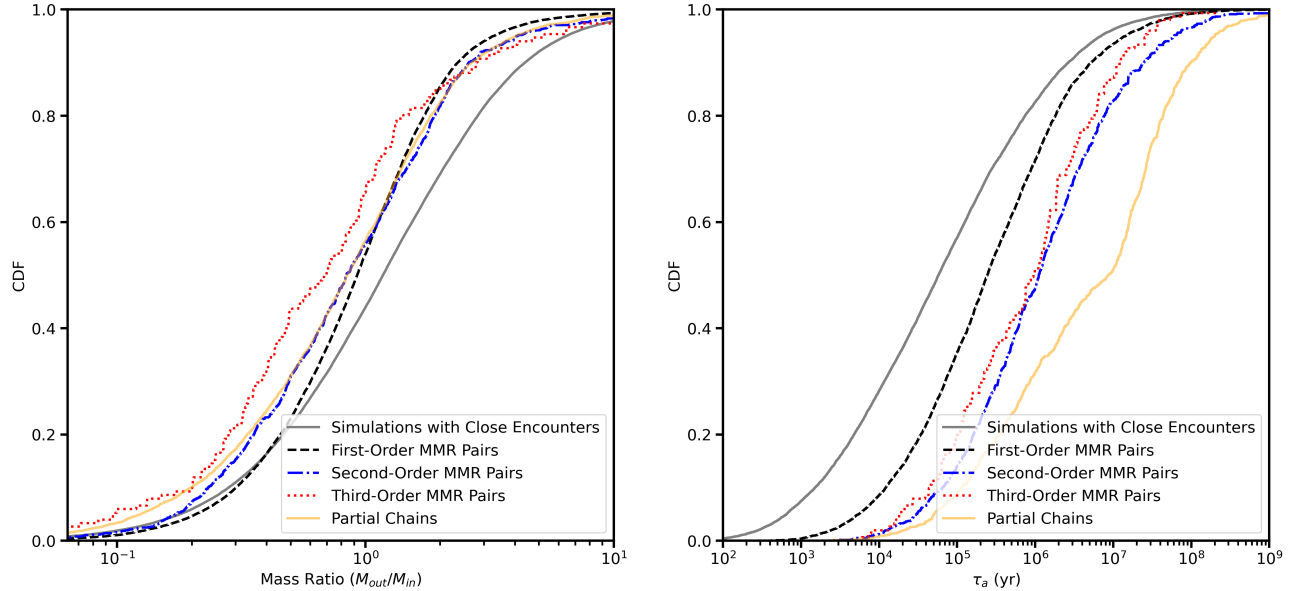
Figure 10. CDFs of the mass ratios and the migration timescales τ_a of the planet pairs in systems that captured into first-, second-, third-order resonance. Systems that experienced close encounters and systems that failed to form complete resonant chains are also shown. Higher-order MMRs preferentially form when the outer planet is less massive and when τ_a is large, both of which are tied to slow migration.

to operate, which means that it happens when the disk is still present and is thus captured by our simulations. The simulation explored in Section 3 is one such example where the innermost planet pair initially captures a 2:1 MMR, which is later disrupted. In fact, since our model for eccentricity damping ignores its dependence on eccentricity, it may have even overestimated the importance of overstability (Xu et al. 2018). On the other hand, there may be some other mechanism that causes eccentricity damping after disk dispersal on longer timescales, such as dynamical interaction with planetesimals (Chatterjee & Ford 2015; Wu et al. 2024).

Regardless, it seems probable that additional mechanisms are required to fully explain the observed paucity of the 2:1 and 3:1 resonances relative to our simulations. One likely source of the difference between simulation and observation is the relevant initial conditions. If real planetary systems start closer to each other than what we assumed in our initial conditions, more pairs would never encounter 2:1 and 3:1, naturally reducing their ocurrence rates. This would be consistent with other observational evidence that low-mass planets may initially form in compact chains (Xu & Wang 2024). In other words, our simulations probbaly do not overestimate the probability for a system to stay resonant after encountering a 2:1 or 3:1 resonance, but we may overestimate the probability for a system to encounter 2:1 and 3:1 in the first place.

This explanation leaves one question: how can our initial period ratio condition be too wide when it was set according to the present-day observations, which, presumably, include planets that have undergone some convergent migration and are thus more compact than the true initial conditions? There are two factors that can contribute to this. First, middle planets may be missed in transit observations since planets in the same system have small but finite mutual inclinations (e.g. Zhu et al. 2018). In other words, an adjacent planet pair with a large period ratio may actually have an intermediate planet, thus decreasing the reported period ratios. Second, a middle planet can be removed (colliding and merging with other planets or escaping the system) through long-term dynamical instability, which may take place during the Gyr evolution after disk dispersal (Izidoro et al. 2017). In these cases, the final separations could be larger than the initial conditions.

4.4. *Higher-Order MMRs Prefer Slower Migration*

The probability of resonance capture strongly increases under adiabatic encounters i.e. the migration timescale should be slower than the resonant interaction timescale (e.g. Henrard 1982; Henrard & Lemaitre 1983; Batygin & Morbidelli 2013). Theoretically, we anticipate that the formation of weaker, higher-order MMRs, which have narrower libration widths and slower libration timescales, demands slower migration than first-order. The differential migration rate between a pair
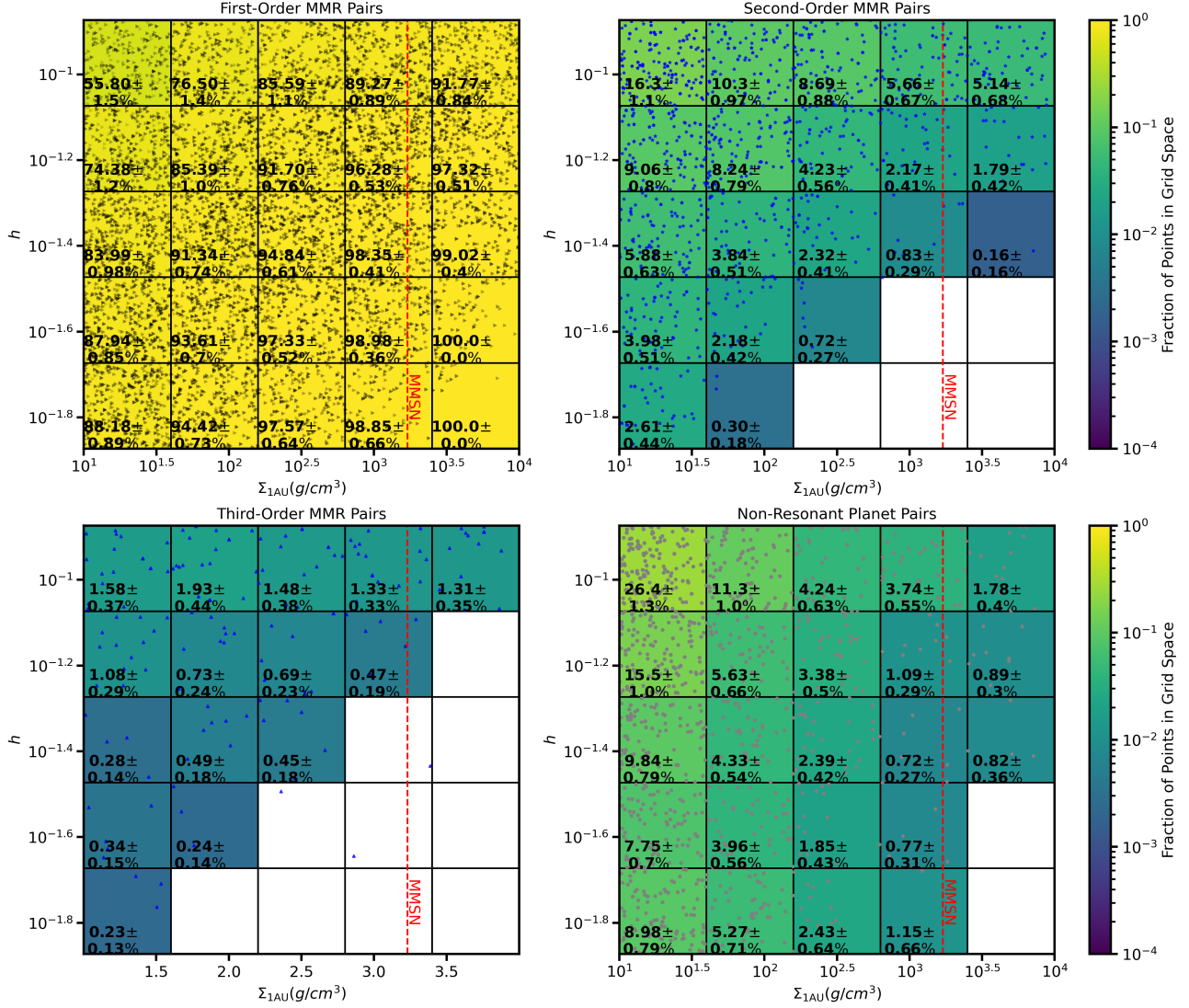
Figure 11. The relative outcome of Type-I disk migration as a function of disk surface density (Σ_{1AU}) and disk aspect ratio (h). The four panels show planets that captured into first-, second-, and third-order MMR as well as non-resonant planets. For reference, a dotted red line marks the surface density of the Minimum Mass Solar Nebula (Hayashi 1981). Higher-order resonances prefer low Σ_{1AU} and high h, both of which slow down migration (Eqn. 5). Low Σ_{1AU} may correspond to transitional disks or truncated disks; the formation of Kepler-like planets in such disks has been proposed previously (Lee & Chiang 2016; Dupuy et al. 2016).

of planets is set by the mass ratios between the planets (heavier planets tend to migrate faster) and the local disk properties (Eqn. 3).

In Fig. 10, we show the cumulative distribution functions of the mass ratios between neighboring planets and the migration rates for planets that ended up in MMRs of different orders. The mass ratio of neighboring planets m_{out}/m_{in} are consistent with being around unity $log(m_{out}/m_{in}) = 0.0 \pm 0.4$ for pairs that ended up in first-order resonances, while the distribution for higher-order resonance shows a subtle preference smaller than unity $log(m_{out}/m_{in}) = -0.1 \pm 0.4$. Indeed, a smaller

outer planet leads to slower differential migration between the planets and thus favors capture into resonance. However, given how subtle the difference is, we do not expect any observable difference in the mass ratios for planets in higher-order resonances from those in first-order resonances. Goyal & Wang (2022) reported that intra-system uniformity in planetary mass appears to be stronger in observed resonant systems i.e. neighboring planets are similar in size.

Xu & Lai (2017) also proposed that planets in second-order MMRs should have order unity mass ratios: $m_{out}/m_{in} \sim 1$. This result follows because, on the
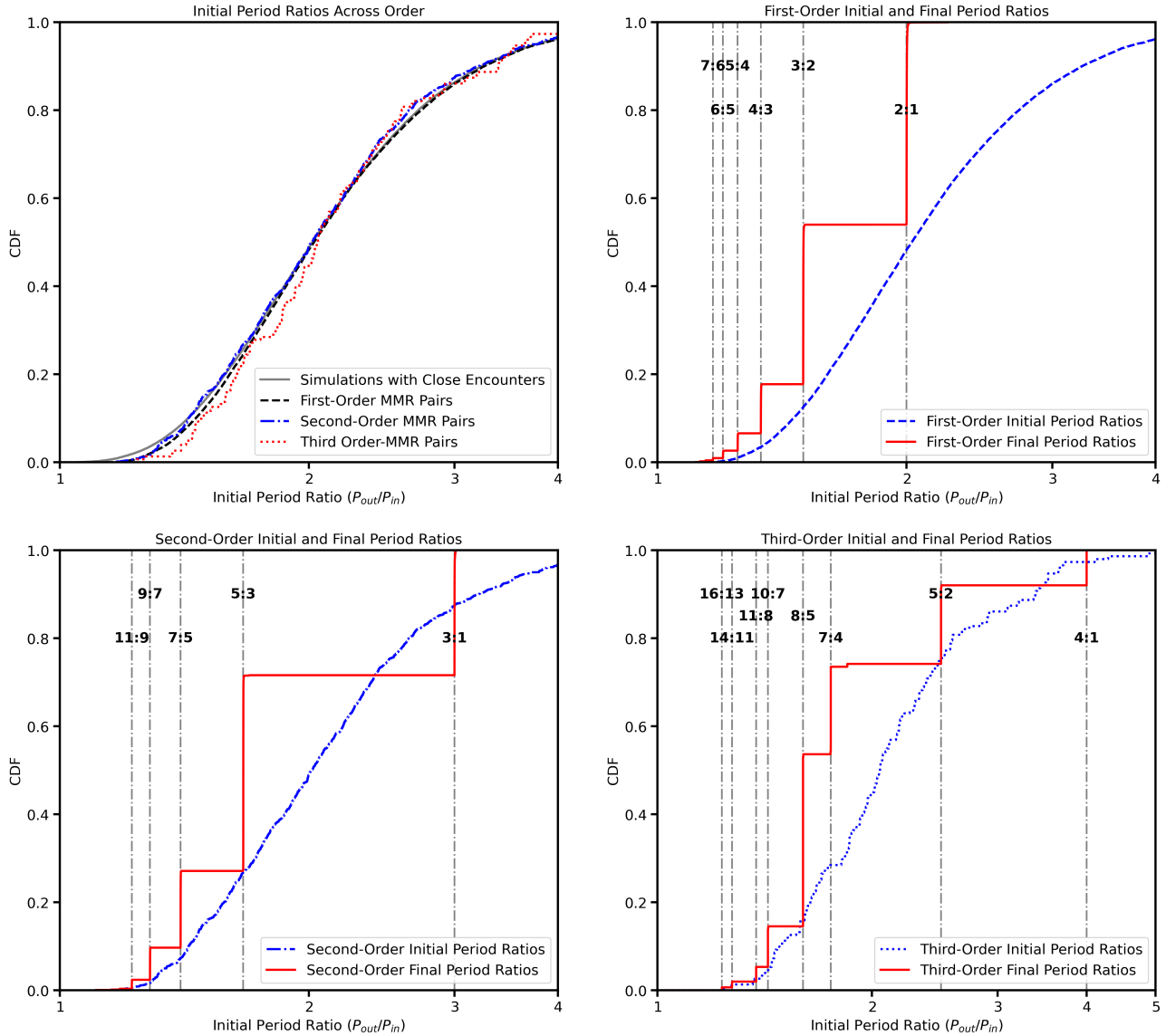
Figure 12. Top left: CDF of the initial period ratios of the planet pairs that captured into first-, second-, and third-order MMR. The remaining three panels show the initial period ratios and final period ratios for each order. Notice that a planet pair that end up in a higher-order MMR need not begin with a commensurate period ratio.

one hand, convergent migration requires a massive outer planet ($m_{out}/m_{in} > 1$), but, on the other, the stability of a captured resonance demands $m_{out}/m_{in} < 1$ to avoid overstable libration. Our simulations are broadly consistent with this result, and the stability criterion may have contributed to the preference for lower m_{out}/m_{in}, but our mass ratio distribution is wider: it spans almost half a dex ($log(m_{out}/m_{in}) = -0.1 \pm 0.4$). We argue that this is because the disk inner edge was crucial for converting divergent encounters into convergent ones by stopping the migration of the inner planets, making it possible for a less massive outer planet to catch up. Moreover, in a resonant chain, neighboring resonances may also

help stabilize a higher-order MMR e.g. through three-body Laplace-like resonance (Agol et al. 2021). Indeed, 79.3% of higher-order two-body MMRs participate in at least one three-body resonance. Xu & Lai (2017) only considered isolated pairs of planets.

Slower migration favors the capture into higher-order resonces. The average migration τ_a is larger for higher-order resonance than first-order: $\tau_a = 10^{3.0\pm1.0}$ kyr v.s. $\tau_a = 10^{2.4\pm1.0}$ kyr (see Tab. 3 and Fig. 10). Although the two distributions overlap substantially, our simulated sample of 6000 systems provide enough statistical power to differentiate them in a Kolmogorov—Smirnov (KS) test (Berger & Zhou 2014) (5σ). Translated to
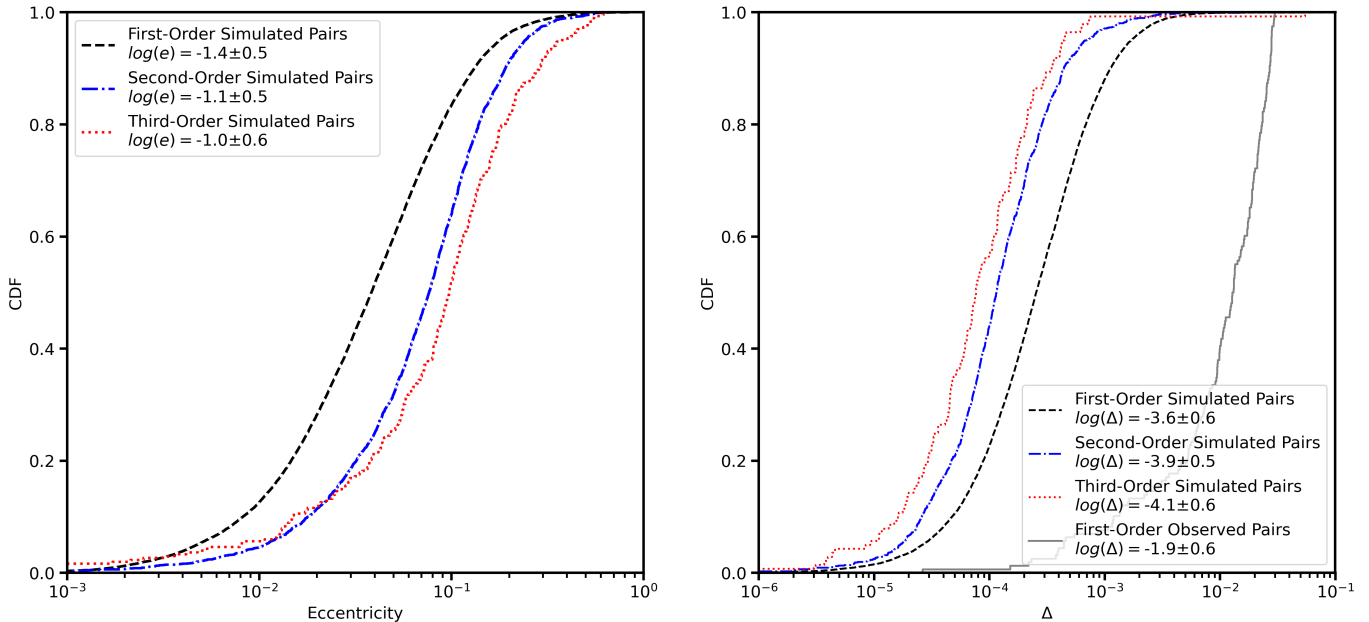
Figure 13. CDFs of eccentricities and Δ for planets that captured into first-, second-, and third-order MMRs. Higher-order MMRs have smaller Δ than first-order resonances (KS tests confirmed the statistical significance). We also include the Δ distribution of observed planets near first-order resonances (gray). The Δ of observed systems are substantially larger than the simulated ones. The observed systems likely have circulating resonant angles (Goldberg & Batygin 2023).

Σ and h, higher-order resonances prefer lower disk surface densities and larger disk aspect ratio: $\Sigma_{1AU} = 10^{1.8\pm0.8}$g cm^{-2} v.s.$\Sigma_{1AU} = 10^{2.3\pm0.8}$g cm^{-2}; $h = 10^{-1.0\pm0.2}$ v.s. $h = 10^{-1.3\pm0.3}$. In Fig. 11, we display the 2-D parameter space of Σ-h and show where higher-order resonances tend to emerge. The MMSN (Hayashi 1981) is labeled for comparison.

4.5. Higher-Order MMRs do not Require Commensurate Initial Period Ratios

One might naively expect that the planets that end up in higher-order MMR were initialized with a period ratio commensurate with the final resonance, avoiding intervening stronger first-order MMRs.

After a short migration, these planets could have captured into the nearby higher-order MMR. In previous simulations of resonant chains, this approach was adopted to capture planets into a series of pre-determined resonances (e.g., Huang & Ormel 2022; Pichierri et al. 2018; Tamayo et al. 2017; Lammers & Winn 2024).

In our simulations, we found that higher-order MMRs do not require initial period ratios that are commensurate with the final resonance. Specifically, only 43 out of the second-order 1124 pairs started with a period ratio within 2% of the final resonance. Similarly, only 6 out of the 151 third-order pairs started with near-commensurate period ratios. In Fig. 12, we show the

cumulative distributions of the initial period ratios for all planet pairs that end up in first-, second-, and third-order MMRs separately. We found the different orders had statistically indistinguishable initial period ratios. The p-values from a KS test (Berger & Zhou 2014) between the first and second-order was 0.2, and between first and third-order were 0.4. Moreover, there are no discernible peaks in the initial period distribution near the final resonances (Fig. 12).

The explanation is simple: most higher-order MMR have to undergo substantial migration. The pair likely briefly resided in a first-order MMR before breaking away and capturing into a nearby higher-order resonance as discussed in the case study of Section 3. A quick examination of ~ 100 systems suggests that around half of higher-order MMRs form through this pathway. In this scenario, the initial period ratios hardly matter.

4.6. Higher-Order MMRs Have Smaller Δ, Higher e

In our simulations, the planets in higher-order MMRs indeed have larger equilibrium eccentricities than their first-order counterparts. This result is shown in Fig. 13, where KS tests suggest that the eccentricity distributions of higher-order resonances are statistically different from that of first-order $> 5\sigma$. The eccentricities are $\log(e) = -1.4 \pm 0.5$ for first-order MMR, $\log(e) = -1.1 \pm 0.5$ for second-order, and $\log(e) = -1.0 \pm 0.6$ for third-order. Again, this is because slower eccentricity

damping imparts a non-zero eccentricity before planets encounter higher-order MMR and favors capture (see Section 4.2).

The high eccentricities for higher-order resonances may lead to resonance overlap and orbital instability after the disk dissipates (e.g. Lammers et al. 2024; Petit et al. 2020; Tamayo et al. 2021; Hadden & Lithwick 2018; Deck et al. 2013). Higher-order MMR may be the weakest link of a resonant chain and contribute to the breaking of chains (Dai et al. 2023). We defer a dynamical stability analysis of our simulated higher-order MMR to a future work.

The right panel of Fig. 13 shows the distribution of Δ for simulated planets in first-order MMR and higher-order MMR, as well as the observed Δ among confirmed exoplanets. The first-order MMRs have $\log(\Delta) = -3.6 \pm 0.6$, second-order MMRs are slightly deeper with $\log(\Delta) = -3.9 \pm 0.5$, and third-order MMRs are half a dex removed from first-order, $\log(\Delta) = -4.1 \pm 0.6$. Again, KS tests confirm that the difference in these Δ distributions are statistically significant $> 5\sigma$. This result is consistent with existing literature on second-order resonances. The libration for at least second-order MMRs is symmetric in period ratio which, when time averaged, corresponds to smaller Δ values (Bailey et al. 2022).

Relative to the simulated in resonant pairs, observed, near-resonant planets have Δ values that deviate further zero: observed first-order MMRs have $\log(\Delta) = -1.9 \pm 0.6$ (or 1-2%, Fabrycky et al. 2014). The majority of near-resonant planets have circulating resonant angles and are thus only near-resonant (Hadden & Lithwick 2017; Goldberg & Batygin 2023). Multiple mechanisms have been invoked to push the initially resonant planets out of resonance including orbital instability (e.g. Li et al. 2024), disk turbulence (e.g. Goldberg & Batygin 2023), disk edge expansion (e.g. Liu et al. 2017; Hansen et al. 2024), obliquity tides (Millholland & Laughlin 2019; Louden et al. 2021), planetesimal scatterings (e.g. Chatterjee & Ford 2015; Wu et al. 2024), and post-formation divergent encounters (e.g. Lin et al. 2024).

4.7. *Innermost Pairs More Likely Form Higher-Order MMRs*

We found that higher-order MMRs tend to form on the innermost planet pair of a resonant chain (see example systems in Fig. 4). Given the adopted multiplicity of planets (3-7) in our simulations, the innermost pairs represent 25.9% of all neighboring pairs. The formation of strong first-order resonance seem to be agnostic about the relative location of the planet pair in a resonant

chain: the innermost pair account for $5786/22444 = 25.8\%$ of first-order MMR. The fraction of innermost pairs engaged in a higher-order MMR is significantly higher, $419/1124 = 37.3\%$ and $63/151 = 41.7\%$ for second- and third-order MMR respectively.

Planets in the innermost pair are more likely to break from the first MMR because this pair of planets are pushed from both sides in our simulations. The innermost planet is typically at the disk inner edge, so the net migration is outward. The second to innermost planet migrates inwards. Moreover, there is often a whole chain of planets locked in resonance whose net migration are all inwards. As the innermost pair is squeezed, a previously established first-order resonance can break and subsequent migration can capture that pair into a nearby higher-order MMR. This pattern is essentially what happened in the case studies in Section 3. That said, longer-period planets can still form higher-order MMR. This is both seen in our simulations and in observations, e.g. TOI-1136 ef (Dai et al. 2023).

4.8. *Planets Can be Pushed Inside the Inner Disk Edge*

In our simple prescription of Type-I migration with an inner disk edge, the innermost planet is solely responsible for halting the chain's inward migration. This is because the net migration torque is reversed in a narrow region of 0.01 AU centered at 0.05 AU where typically only one planet can reside. We found that in $\sim 10\%$ of our simulations, the innermost planet is pushed by longer-period planets through the disk inner edge. Lower-mass innermost planets are particularly susceptible to being pushed through the disk edge. Fig. 14 shows that the planets that stopped at the disk edge have a typical mass of $\log(M_p/M_\oplus) = 0.8 \pm 0.4$ or $M_p = 4\text{-}15\ M_\oplus$, whereas the planets that failed to stop the inward migration is $\log(M_p/M_\oplus) = 0.2 \pm 0.4$ or $M_p = 0.5\text{-}4\ M_\oplus$. Interestingly, although the average libration amplitude of the innermost planet pair is slightly lower in systems where the innermost planet crosses the inner disk edge, both distributions have a median near 0. This result indicates that the majority of planets that pass through the inner disk edge still capture into mean-motion resonances. Indeed, the median libration amplitude for planet pairs with a planet that passes through the disk inner edge is 1.04 degrees, which significantly below the threshold for circulation but still elevated from the median value for planets that do not cross the edge, 0.38 degrees.

Admittedly, the above results are contingent on the validity of our simple treatment of the disk inner edge. More realistic hydrodynamic simulations (e.g. Wu et al. 2024; Yang & Li 2024; Ataiee & Kley 2021b) are required to resolve the detailed planet-disk interaction

Table 1. Factors that Promote Higher-order MMRs

Factor	Higher-order MMR	First-order MMR
Larger $log(\tau_a/kyr)$	3.0 ± 1.0	2.4 ± 1.0
Smaller $log(m_{out}/m_{in})$	-0.1 ± 0.5	-0.0 ± 0.4
Smaller $log(\Sigma/g\ cm^{-2})$	1.8 ± 0.8	2.3 ± 0.8
Larger $log(h)$	-1.1 ± 0.2	-1.3 ± 0.3
Smaller $log(K)$	1.5 ± 0.5	2.0 ± 0.5

and density wave interferences at the inner disk. Even within tested hydrodynamic simulations, the mechanism of capture at the cavity and the maximum torque generated by this trap are uncertain (Miranda & Lai 2018; Liu et al. 2017). Recent studies have highlighted the importance of planets crossing the inner disk edge in establishing the final orbital architecture of the system. These works tend to suggest that the disk itself would recess (Pichierri et al. 2024; Huang & Ormel 2022; Liu et al. 2022, 2017).
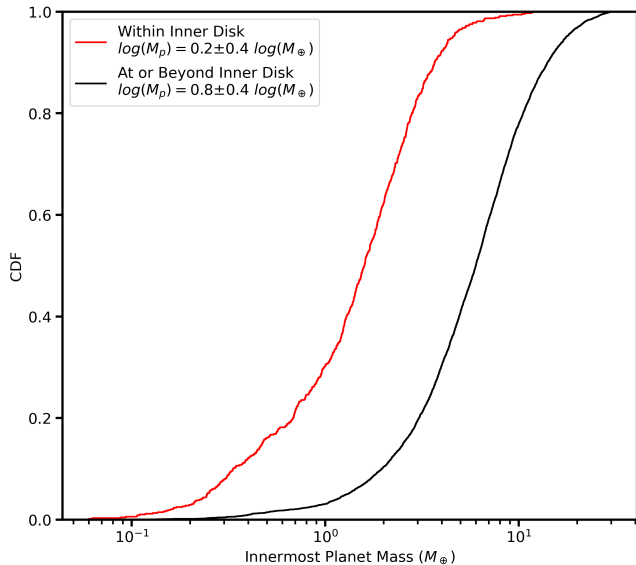
Figure 14. Cumulative distribution functions (CDF) comparison of the mass distribution of innermost planets that pass through the disk inner edge ($a_0 < 0.049$ AU) versus all other converged systems. Reported uncertainties correspond to 1σ deviations.

5. CONCLUSION

In this paper, we investigated the formation of second- and third-order MMRs during Type-I migration with an inner disk edge. We ran more than 6000 simulations using the `type_I_migration` (Kajtazi et al. 2023) scheme in `REBOUNDx` (Tamayo et al. 2020; Rein & Liu 2012).

Our simulations aimed to reproduce the observed stellar mass, planet radius/mass, multiplicity, and intra-system uniformity of Kepler-like planets (e.g. Fabrycky et al. 2014; Weiss et al. 2018; Millholland et al. 2017b; Wang 2017; Zhu & Dong 2021). We included a wide set of protoplanetary disk surface densities $10 - 10^4$ g cm^{-2} at 1AU and aspect ratios $H/R = 0.1 - 0.01$. This range may encompass transitional or truncated disks (Lee & Chiang 2016; Dupuy et al. 2016) i.e. during the last stage of planet formation when the resonant chains are assembled. Our findings are as follows:

1. Among > 6000 simulated systems, $\sim 5\%$ and $\sim 0.5\%$ of resonant planet pairs were captured into second- and third-order MMRs (in a state of libration); $\sim 13\%$ and $\sim 2\%$ of systems contain at least one second-order or third-order MMR.

2. Even though the above fractions depended on the assumed disk properties, the fraction of individual resonances (e.g. 5:3 v.s. 7:5) in our simulations very well reproduced that of the observed sample Dai et al. (2024). MMRs with tight period ratio spacings are increasingly rare (Tab. 4), as a pair of planets have to avoid being captured into all preceding resonances. $2:1$ and $3:1$ resonances are significantly more common in our simulations than in the observed sample, likely because of observational biases or the fact that 2:1 and 3:1 are particularly prone to overstability.

3. As predicted by theory (Xu & Lai 2017), higher-order MMRs more likely emerge in lower-density disks ($\Sigma_{1AU} = 10^{1.8\pm0.8}$g cm^{-2} v.s. $\Sigma_{1AU} = 10^{2.3\pm0.8}$g cm^{-2} for first-order). The distinction in disk density is small enough that we expect to find higher-order MMRs in the same observational sample as first-order resonances.

4. A pair of planets can capture into a higher-order MMR even (and perhaps especially) when there is an intervening first-order resonance. Specifically, only 43 out of the second-order 1124 pairs and 6

of 151 third-order pairs started with a period ratio within 2% of the final resonance. Planets typically enter a "stronger" first-order MMR before breaking away and gently capturing into a nearby higher-order resonance. The initial period ratio is not the sole defining factor of the selection of the order of MMR.

5. Higher-order MMR do not have to form as part of a pre-existing Laplace-like three-body resonance. The majority of our higher-order MMRs form through two-body resonances.

6. Instead, we suggest that small but non-zero pre-capture eccentricities caused by a prior first-order resonance facilitate the capture into higher-order MMR.

Based on our simulations, we also make some predictions about higher-order MMRs in observed systems:

1. The formation of higher-order MMRs prefers disks that cause slow migration. Many of the simulated systems with higher-order MMRs have longer-period planets that have yet to reach the inner disk whereas rapid disk migration mostly gives rise to complete first-order resonant chains where all planets have completed migration. We predict that higher-order MMR planets are more likely to occur in systems with longer-period non-resonant planets.

2. The absolute frequency of higher-order MMRs depends on disk properties, but higher-order MMRs are rare. They should tend to appear as an isolated pair in an otherwise first-order resonant chain.

3. The inner pairs of a resonant chain are more likely engaged in higher-order MMR. This is because outward migration on the innermost planet and inward migration of all longer-period planets tend to squeeze this pair and break it. Breaking from resonance gives the planets another chance to capture into nearby higher-order resonance.

4. Slower eccentricity damping help maintain a non-zero pre-capture eccentricities which in turn facilitate the capture into higher-order MMR. In our simulations, higher-order MMRs tend to have higher equilibrium eccentricities: $\log(e) = -1.4 \pm 0.5$ for first-order MMR, $\log(e) = -1.1 \pm 0.5$ for second-order, and $\log(e) = -1.0 \pm 0.6$ for

third-order resonance. Such high eccentricities for higher-order resonances may lead to resonance overlap and orbital instability after the disk dissipates (e.g. Lammers et al. 2024; Petit et al. 2020; Tamayo et al. 2021; Hadden & Lithwick 2018; Deck et al. 2013). We predict young planets in higher-order MMR may have e as high as 0.1, higher than that of mature planets (Hadden & Lithwick 2017, e.g. ≈ 0.05).

We acknowledge that effects such as disk turbulence (Adams et al. 2008; Goldberg & Batygin 2023; Wu et al. 2024), disk evolution (Pichierri et al. 2024; Hansen et al. 2024; Huang & Ormel 2022; Liu et al. 2017), the collisional growth/gas accretion of planets (Izidoro et al. 2017), and density wave interaction (Yang & Li 2024) have not been accounted for in our simulations. Post-formation dynamical evolution of these systems is the obvious next step. Higher-order MMRs may play an important role in the disruption of resonant chains (Pichierri & Morbidelli 2020; Goldberg & Batygin 2022; Izidoro et al. 2017; Goldberg et al. 2022; Li et al. 2024). We defer such an investigation to a future study.

Software: REBOUND (Rein & Liu 2012), REBOUNDx (Tamayo et al. 2020), celmech (Hadden & Tamayo 2022), forecaster (Chen & Kipping 2017), pandas (Pandas Development Team 2020; Wes McKinney 2010), numpy (Harris et al. 2020), scipy (Virtanen et al. 2020), astropy (Astropy Collaboration et al. 2022), Matplotlib (Hunter 2007), Seaborn (Waskom 2021), label-lines (Cadiou 2022)

REFERENCES

Adams, F. C., Laughlin, G., & Bloch, A. M. 2008, ApJ, 683, 1117, doi: 10.1086/589986

Agol, E., Dorn, C., Grimm, S. L., et al. 2021, Planetary Science Journal, 2, doi: 10.3847/PSJ/abd022

Andrews, S. M. 2020, ARA&A, 58, 483, doi: 10.1146/annurev-astro-031220-010302

Astropy Collaboration, Price-Whelan, A. M., Lim, P. L., et al. 2022, ApJ, 935, 167, doi: 10.3847/1538-4357/ac7c74

Ataiee, S., & Kley, W. 2021a, Astronomy & Astrophysics, 648, A69

—. 2021b, A69

Bailey, N., Gilbert, G., & Fabrycky, D. 2022, AJ, 163, 13, doi: 10.3847/1538-3881/ac2f46

Batygin, K. 2015, Monthly Notices of the Royal Astronomical Society, 451, 2589, doi: 10.1093/mnras/stv1063

Batygin, K., Adams, F. C., & Becker, J. 2023, ApJL, 951, L19, doi: 10.3847/2041-8213/acdb5d

Batygin, K., & Morbidelli, A. 2013, A&A, 556, A28, doi: 10.1051/0004-6361/201220907

Berger, V. W., & Zhou, Y. 2014, Wiley statsref: Statistics reference online

Cadiou, C. 2022, Matplotlib label lines, Zenodo, doi: 10.5281/ZENODO.7428070

Carter, J. A., Agol, E., Chaplin, W. J., et al. 2012, Science, 337, 556

Chatterjee, S., & Ford, E. B. 2015, The Astrophysical Journal, 803, 33, doi: 10.1088/0004-637x/803/1/33

Chen, J., & Kipping, D. 2017, ApJ, 834, 17, doi: 10.3847/1538-4357/834/1/17

Chiang, E., & Laughlin, G. 2013, MNRAS, 431, 3444, doi: 10.1093/mnras/stt424

Chiang, E. I., Lovering, J. R., Millis, R. L., et al. 2003, Earth, Moon, and Planets, astro, doi: 10.1023/B:MOON.0000031924.20073.d0

Choksi, N., & Chiang, E. 2020, Monthly Notices of the Royal Astronomical Society, 495, 4192

Coleman, G. A., Leleu, A., Alibert, Y., & Benz, W. 2019, Astronomy & Astrophysics, 631, A7

Cresswell, P., & Nelson, R. P. 2008, A&A, 482, 677, doi: 10.1051/0004-6361:20079178

Cresswell, P., & Nelson, R. P. 2008, Astronomy & Astrophysics, 482, 677

Dai, F., Winn, J. N., Schlaufman, K., et al. 2020, AJ, 159, 247, doi: 10.3847/1538-3881/ab88b8

Dai, F., Masuda, K., Beard, C., et al. 2023, The Astronomical Journal, 165, 33

Dai, F., Goldberg, M., Batygin, K., et al. 2024, The Astronomical Journal, 168, 239, doi: 10.3847/1538-3881/ad83a6

Deck, K. M., & Batygin, K. 2015, ApJ, 810, 119, doi: 10.1088/0004-637X/810/2/119

Deck, K. M., Payne, M., & Holman, M. J. 2013, The Astrophysical Journal, 774, 129

DeMeo, F., & Carry, B. 2013, Icarus, 226, 723

Dupuy, T. J., Kratter, K. M., Kraus, A. L., et al. 2016, ApJ, 817, 80, doi: 10.3847/0004-637X/817/1/80

Fabrycky, D. C., Ford, E. B., Steffen, J. H., et al. 2012, ApJ, 750, 114, doi: 10.1088/0004-637X/750/2/114

Fabrycky, D. C., Lissauer, J. J., Ragozzine, D., et al. 2014, ApJ, 790, 146, doi: 10.1088/0004-637X/790/2/146

Gillon, M., Triaud, A. H. M. J., Demory, B.-O., et al. 2017, Nature, 542, 456, doi: 10.1038/nature21360

Goldberg, M., & Batygin, K. 2021, The Astronomical Journal, doi: 10.3847/1538-3881/abfb78

—. 2022, The Astronomical Journal, doi: 10.3847/1538-3881/ac5961

Goldberg, M., & Batygin, K. 2023, ApJ, 948, 12, doi: 10.3847/1538-4357/acc9ae

Goldberg, M., Batygin, K., & Morbidelli, A. 2022, arXiv e-prints, arXiv:2207.13833. https://arxiv.org/abs/2207.13833

Goldreich, P., & Schlichting, H. E. 2014, AJ, 147, 32, doi: 10.1088/0004-6256/147/2/32

Goldreich, P., & Tremaine, S. 1979, ApJ, 233, 857, doi: 10.1086/157448

Goyal, A. V., & Wang, S. 2022, ApJ, 933, 162, doi: 10.3847/1538-4357/ac7562

Hadden, S. 2019a, AJ, 158, 238, doi: 10.3847/1538-3881/ab5287

—. 2019b, AJ, 158, 238, doi: 10.3847/1538-3881/ab5287

Hadden, S., & Lithwick, Y. 2017, AJ, 154, 5, doi: 10.3847/1538-3881/aa71ef

Hadden, S., & Lithwick, Y. 2018, The Astronomical Journal, doi: 10.3847/1538-3881/aad32c

Hadden, S., & Tamayo, D. 2022, The Astronomical Journal, 164, 179

Haisch Jr, K. E., Lada, E. A., & Lada, C. J. 2001, The Astrophysical Journal, 553, L153

Hamer, J. H., & Schlaufman, K. C. 2024, The Astronomical Journal, 167, 55

Hansen, B. M. S., Yu, T.-Y., & Hasegawa, Y. 2024, The Open Journal of Astrophysics, 7, doi: 10.33232/001c.121410

Harris, C. R., Millman, K. J., van der Walt, S. J., et al. 2020, Nature, 585, 357, doi: 10.1038/s41586-020-2649-2

Hayashi, C. 1981, Progress of Theoretical Physics Supplement, 70, 35, doi: 10.1143/PTPS.70.35

He, M. Y., & Ford, E. B. 2022, AJ, 164, 210, doi: 10.3847/1538-3881/ac93f4

Henrard, J. 1982, Celestial Mechanics, vol. 27, May 1982, p. 3-22., 27, 3

Henrard, J., & Lemaitre, A. 1983, Celestial mechanics, 30, 197

Henrard, J., Lemaitre, A., Milani, A., & Murray, C. D. 1986, Celestial Mechanics, 38, 335, doi: 10.1007/BF01238924

Huang, S., & Ormel, C. W. 2022, MNRAS, 511, 3814, doi: 10.1093/mnras/stac288

Huang, S., & Ormel, C. W. 2023, Monthly Notices of the Royal Astronomical Society, 522, 828

Hunter, J. D. 2007, Computing in Science & Engineering, 9, 90, doi: 10.1109/MCSE.2007.55

Izidoro, A., Ogihara, M., Raymond, S. N., et al. 2017, MNRAS, 470, 1750, doi: 10.1093/mnras/stx1232

Jontof-Hutter, D., Rowe, J. F., Lissauer, J. J., Fabrycky, D. C., & Ford, E. B. 2015, Nature, 522, 321, doi: 10.1038/nature14494

Kajtazi, K., Petit, A. C., & Johansen, A. 2023, Astronomy & Astrophysics, 669, A44

Kley, W., & Nelson, R. P. 2012, ARA&A, 50, 211, doi: 10.1146/annurev-astro-081811-125523

Lammers, C., Hadden, S., & Murray, N. 2024, The Astrophysical Journal, 972, 53

Lammers, C., & Winn, J. N. 2024, The Astrophysical Journal Letters, 968, L12

Lee, E. J., & Chiang, E. 2016, ApJ, 817, 90, doi: 10.3847/0004-637X/817/2/90

Leleu, A., Alibert, Y., Hara, N., et al. 2021, Astronomy & Astrophysics, 649, A26

Li, M., & Xiao, L. 2016, The Astrophysical Journal, 820, 36

Li, R., Chiang, E., Choksi, N., & Dai, F. 2024, arXiv e-prints, arXiv:2408.10206, doi: 10.48550/arXiv.2408.10206

Lin, D. N. C., & Papaloizou, J. 1986, ApJ, 309, 846, doi: 10.1086/164653

Lin, J., Dudiak, I., Hadden, S., & Tamayo, D. 2024, arXiv e-prints, arXiv:2412.12415, doi: 10.48550/arXiv.2412.12415

Liu, B., Ormel, C. W., & Lin, D. N. 2017, Astronomy & Astrophysics, 601, A15

Liu, B., Ormel, C. W., & Lin, D. N. C. 2017, A&A, 601, A15, doi: 10.1051/0004-6361/201630017

Liu, B., Raymond, S. N., & Jacobson, S. A. 2022, Nature, 604, 643, doi: 10.1038/s41586-022-04535-1

Long, F., Pascucci, I., Houge, A., et al. 2025, The Astrophysical Journal Letters, 978, L30

Louden, E. M., Winn, J. N., Petigura, E. A., et al. 2021, AJ, 161, 68, doi: 10.3847/1538-3881/abcebd

Luque, R., Osborn, H. P., Leleu, A., et al. 2023, Nature, 623, 932, doi: 10.1038/s41586-023-06692-3

MacDonald, M. G., Ragozzine, D., Fabrycky, D. C., et al. 2016, AJ, 152, 105, doi: 10.3847/0004-6256/152/4/105

Masset, F. S., Morbidelli, A., Crida, A., & Ferreira, J. 2006, The Astrophysical Journal, 642, 478, doi: 10.1086/500967

Matsumoto, Y., Nagasawa, M., & Ida, S. 2012, Icarus, 221, 624, doi: 10.1016/j.icarus.2012.08.032

McNally, C. P., Nelson, R. P., Paardekooper, S.-J., & Benítez-Llambay, P. 2019, Monthly Notices of the Royal Astronomical Society, 484, 728

Migaszewski, C., Goździewski, K., & Panichi, F. 2017, MNRAS, 465, 2366, doi: 10.1093/mnras/stw2866

Millholland, S., & Laughlin, G. 2019, Nature Astronomy, 3, 424, doi: 10.1038/s41550-019-0701-7

Millholland, S., Wang, S., & Laughlin, G. 2017a, ApJL, 849, L33, doi: 10.3847/2041-8213/aa9714

—. 2017b, ApJL, 849, L33, doi: 10.3847/2041-8213/aa9714

Millholland, S., Laughlin, G., Teske, J., et al. 2018, AJ, 155, 106, doi: 10.3847/1538-3881/aaa894

Mills, S. M., Fabrycky, D. C., Migaszewski, C., et al. 2016, Nature, 533, 509, doi: 10.1038/nature17445

Mills, S. M., Fabrycky, D. C., Migaszewski, C., et al. 2016, Nature, 533, 509, doi: 10.1038/nature17445

Miranda, R., & Lai, D. 2018, Monthly Notices of the Royal Astronomical Society, 473, 5267

Murray, C. D., & Dermott, S. F. 1999, Solar system dynamics (Cambridge university press)

Ogihara, M., Kokubo, E., Suzuki, T. K., & Morbidelli, A. 2018, Astronomy & Astrophysics, 615, A63

Pandas Development Team, T. 2020, pandas-dev/pandas: Pandas, latest, Zenodo, doi: 10.5281/zenodo.3509134

Papaloizou, J. C. B., & Larwood, J. D. 2000, MNRAS, 315, 823, doi: 10.1046/j.1365-8711.2000.03466.x

Peale, S. J. 1976, ARA&A, 14, 215, doi: 10.1146/annurev.aa.14.090176.001243

Petit, A. C., Petigura, E. A., Davies, M. B., & Johansen, A. 2020, Monthly Notices of the Royal Astronomical Society, 496, 3101

Pichierri, G., & Morbidelli, A. 2020, MNRAS, 494, 4950, doi: 10.1093/mnras/staa1102

Pichierri, G., Morbidelli, A., Batygin, K., & Brasser, R. 2024, Nature Astronomy, 1

Pichierri, G., Morbidelli, A., & Crida, A. 2018, Celestial Mechanics and Dynamical Astronomy

Quinn, T., & MacDonald, M. G. 2023, The Astronomical Journal, 166, 58

Rath, J., Hadden, S., & Lithwick, Y. 2022, The Astrophysical Journal, 932, 61

Rein, H., & Liu, S. F. 2012, A&A, 537, A128, doi: 10.1051/0004-6361/201118085

Rein, H., & Tamayo, D. 2015, Monthly Notices of the Royal Astronomical Society, 452, 376–388, doi: 10.1093/mnras/stv1257

Ribas, Á., Bouy, H., & Merín, B. 2015, Astronomy & Astrophysics, 576, A52

Sessin, W., & Ferraz-Mello, S. 1984, Celestial Mechanics, 32, 307, doi: 10.1007/BF01229087

Shapiro, S. L., & Teukolsky, S. A. 1983, Black Holes, White Dwarfs, and Neutron Stars: The Physics of Compact Objects (Wiley), doi: 10.1002/9783527617661

Siegel, J. C., & Fabrycky, D. 2021, The Astronomical Journal, 161, 290, doi: 10.3847/1538-3881/abf8a6

Silverberg, S. M., Wisniewski, J. P., Kuchner, M. J., et al. 2020, The Astrophysical Journal, 890, 106

Smirnov, E. 2025, Icarus, 116584

Smith, A. W., & Lissauer, J. J. 2009, Icarus, 201, 381

Steffen, J. H., & Hwang, J. A. 2015, MNRAS, 448, 1956, doi: 10.1093/mnras/stv104

Tamayo, D., & Hadden, S. 2024, arXiv e-prints, arXiv:2410.21748, doi: 10.48550/arXiv.2410.21748

Tamayo, D., Murray, N., Tremaine, S., & Winn, J. 2021, The Astronomical Journal, 162, 220

Tamayo, D., Rein, H., Petrovich, C., & Murray, N. 2017, The Astrophysical Journal Letters, 840, L19, doi: 10.3847/2041-8213/AA70EA

Tamayo, D., Rein, H., Shi, P., & Hernandez, D. M. 2020, MNRAS, 491, 2885, doi: 10.1093/mnras/stz2870

Turtelboom, E. V., Dietrich, J., Dressing, C. D., & Harada, C. K. 2024, arXiv preprint arXiv:2409.03852

Virtanen, P., Gommers, R., Oliphant, T. E., et al. 2020, Nature Methods, 17, 261, doi: 10.1038/s41592-019-0686-2

Volk, K., & Malhotra, R. 2025, in Machine Learning for Small Bodies in the Solar System (Elsevier), 173–207

Wang, S. 2017, Research Notes of the American Astronomical Society, 1, 26, doi: 10.3847/2515-5172/aa9be5

Ward, W. R. 1997, Icarus, 126, 261, doi: 10.1006/icar.1996.5647

Waskom, M. L. 2021, Journal of Open Source Software, 6, 3021, doi: 10.21105/joss.03021

Weiss, L. M., Isaacson, H. T., Marcy, G. W., et al. 2018, The Astronomical Journal, 156, 254

Weiss, L. M., Isaacson, H. T., Marcy, G. W., et al. 2018, ArXiv e-prints. https://arxiv.org/abs/1808.03010

Wes McKinney. 2010, in Proceedings of the 9th Python in Science Conference, ed. Stéfan van der Walt & Jarrod Millman, 56 – 61, doi: 10.25080/Majora-92bf1922-00a

Wilhelm, M. J., & Portegies Zwart, S. 2022, Monthly Notices of the Royal Astronomical Society, 509, 44

Winn, J. N., & Fabrycky, D. C. 2015, ARA&A, 53, 409, doi: 10.1146/annurev-astro-082214-122246

Wisdom, J. 1986, Celestial Mechanics, 38, 175, doi: 10.1007/BF01230429

Wisdom, J., & Holman, M. 1991, AJ, 102, 1528, doi: 10.1086/115978

Wong, K. H., & Lee, M. H. 2024, AJ, 167, 112, doi: 10.3847/1538-3881/ad1f60

Wu, Y. 2019, ApJ, 874, 91, doi: 10.3847/1538-4357/ab06f8

Wu, Y., Chen, Y.-X., & Lin, D. N. C. 2024, MNRAS, 528, L127, doi: 10.1093/mnrasl/slad183

Wu, Y., Malhotra, R., & Lithwick, Y. 2024, The Astrophysical Journal, 971, 5, doi: 10.3847/1538-4357/ad5a09

Wu, Y., Malhotra, R., & Lithwick, Y. 2024, arXiv e-prints, arXiv:2405.08893, doi: 10.48550/arXiv.2405.08893

Xiang-Gruess, M., & Papaloizou, J. 2015, Monthly Notices of the Royal Astronomical Society, 449, 3043

Xie, J.-W., Dong, S., Zhu, Z., et al. 2016, Proceedings of the National Academy of Science, 113, 11431, doi: 10.1073/pnas.1604692113

Xu, W., & Lai, D. 2017, MNRAS, 468, 3223, doi: 10.1093/mnras/stx668

Xu, W., Lai, D., & Morbidelli, A. 2018, Monthly Notices of the Royal Astronomical Society, 481, 1538

Xu, W., & Wang, S. 2024, The Astrophysical Journal Letters, 962, L4

Yang, H., & Li, Y.-P. 2024, Monthly Notices of the Royal Astronomical Society, 534, 485

Yi, T., Ormel, C. W., Huang, S., & Petit, A. C. 2025, arXiv preprint arXiv:2502.01736

Zhu, W., & Dong, S. 2021, ARA&A, 59, 291, doi: 10.1146/annurev-astro-112420-020055

Zhu, W., Petrovich, C., Wu, Y., Dong, S., & Xie, J. 2018, ApJ, 860, 101, doi: 10.3847/1538-4357/aac6d5

APPENDIX

We provide the parameters for the second-order and third-order example systems described in Section 3 alongside the third-order evolution plot. Additionally, we list the abundances of each resonance observed in our simulations, as detailed in Section 2.4.

Table 2. System Parameters

Planet 0	Planet 1	Planet 2	Planet 3	Planet 4	Planet 5	Planet 6
m_0	m_1	m_2	m_3	m_4	m_5	m_6
$7.95 M_\oplus$	$4.82 M_\oplus$	$8.64 M_\oplus$	$8.55 M_\oplus$	$8.59 M_\oplus$	$4.42 M_\oplus$	$8.67 M_\oplus$
e_0	e_1	e_2	e_3	e_4	e_5	e_6
0.0507	0.175	0.0492	0.0426	0.0442	0.0251	0.0121
a_{0i}	a_{1i}	a_{2i}	a_{3i}	a_{4i}	a_{5i}	a_{6i}
$0.1 AU$	$0.173 AU$	$0.29 AU$	$0.531 AU$	$0.644 AU$	$1.08 AU$	$1.37 AU$
a_{0f}	a_{1f}	a_{2f}	a_{3f}	a_{4f}	a_{5f}	a_{6f}
$0.0501 AU$	$0.0705 AU$	$0.112 AU$	$0.178 AU$	$0.233 AU$	$0.37 AU$	$0.448 AU$
Planet Pair 01	Planet Pair 12	Planet Pair 23	Planet Pair 34	Planet Pair 45	Planet Pair 56	
m_1/m_0	m_2/m_1	m_3/m_2	m_4/m_3	m_5/m_4	m_6/m_5	
0.607	1.79	0.989	1.0	0.515	1.96	
p_{01}/q_{01}	p_{12}/q_{12}	p_{23}/q_{23}	p_{34}/q_{34}	p_{45}/q_{45}	p_{56}/q_{56}	
5/3	2	2	3/2	2	4/3	
$(P_1/P_0)_f$	$(P_2/P_1)_f$	$(P_3/P_2)_f$	$(P_4/P_3)_f$	$(P_5/P_4)_f$	$(P_6/P_5)_f$	
1.6668	2.0004	2.0007	1.5006	2.0021	1.3344	
Δ_{01}	Δ_{12}	Δ_{23}	Δ_{34}	Δ_{45}	Δ_{56}	
$8.0737 \cdot 10^{-5}$	0.00017715	0.00037187	0.00039041	0.0010665	0.00078198	
ϕ_{01}	ϕ_{12}	ϕ_{23}	ϕ_{34}	ϕ_{45}	ϕ_{56}	
$180.0°$	$167.0°$	$201.0°$	$180.0°$	$189.0°$	$179.0°$	
A_{01}	A_{12}	A_{23}	A_{34}	A_{45}	A_{56}	
$0.184°$	$0.0631°$	$0.0656°$	$0.194°$	$0.136°$	$1.23°$	
Planet Triplet 012	Planet Triplet 123	Planet Triplet 234	Planet Triplet 345	Planet Triplet 456		
ϕ_{012}	ϕ_{123}	ϕ_{234}	ϕ_{345}	ϕ_{456}		
$196.0°$	$39.7°$	$237.0°$	$180.0°$	$242.0°$		
A_{012}	A_{123}	A_{234}	A_{345}	A_{456}		
Σ_{1AU}	h	τ_a	Integration Time	Stellar Mass		
$16.6 g/cm^2$	0.0395	$1350 kyr$	$4050 kyr$	$0.89 M_\odot$		

NOTE—Orbital, migration, and MMR parameters for each planet in the example second-order system. Parameters of the planets involved in the second-order resonance are highlighted in red.
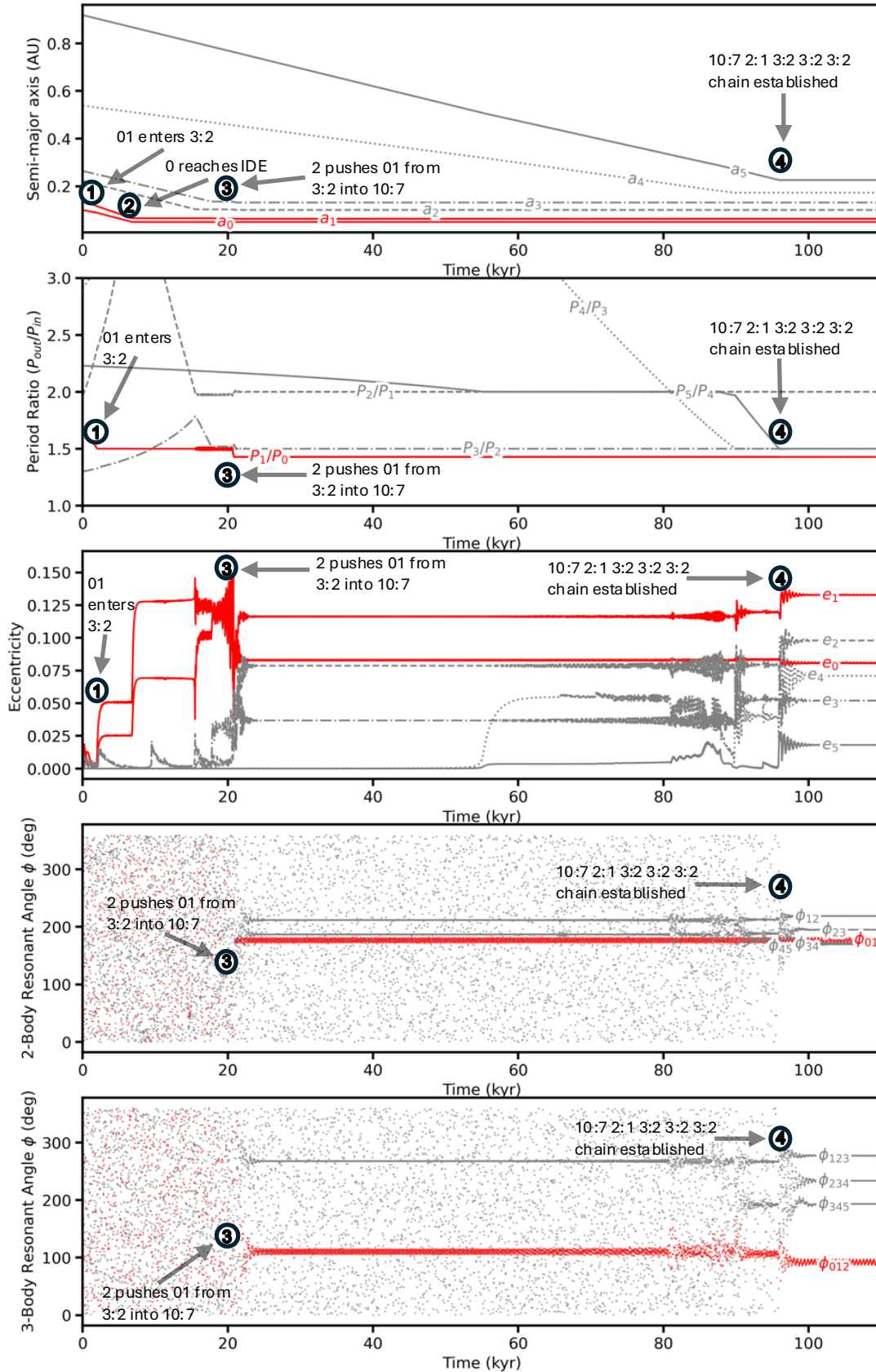
Figure 15. Migration history of a system that ended up with a 10:7 third-order resonance. The innermost two planets entered a first-order 3:2 resonance at milestone (1). At (2), the pair of planets stopped at the inner disk edge. The innermost planet pair broke away from the 3:2 resonance at (3) and quickly settled into the third-order 10:7 resonance. The system eventually became a complete resonant chain at (4).

Table 3. System Parameters

Planet 0	Planet 1	Planet 2	Planet 3	Planet 4	Planet 5
m_0	m_1	m_2	m_3	m_4	m_5
$3.07 M_\oplus$	$6.73 M_\oplus$	$4.03 M_\oplus$	$3.86 M_\oplus$	$2.09 M_\oplus$	$3.93 M_\oplus$
e_0	e_1	e_2	e_3	e_4	e_5
0.0808	0.133	0.0979	0.052	0.0709	0.0181
a_{0i}	a_{1i}	a_{2i}	a_{3i}	a_{4i}	a_{5i}
$0.1 AU$	$0.141 AU$	$0.222 AU$	$0.264 AU$	$0.538 AU$	$0.919 AU$
a_{0f}	a_{1f}	a_{2f}	a_{3f}	a_{4f}	a_{5f}
$0.0499 AU$	$0.0633 AU$	$0.1 AU$	$0.132 AU$	$0.173 AU$	$0.226 AU$
Planet Pair 01	Planet Pair 12	Planet Pair 23	Planet Pair 34	Planet Pair 45	
m_1/m_0	m_2/m_1	m_3/m_2	m_4/m_3	m_5/m_4	
2.19	0.599	0.959	0.541	1.88	
p_{01}/q_{01}	p_{12}/q_{12}	p_{23}/q_{23}	p_{34}/q_{34}	p_{45}/q_{45}	
10/7	2	3/2	3/2	3/2	
$(P_1/P_0)_f$	$(P_2/P_1)_f$	$(P_3/P_2)_f$	$(P_4/P_3)_f$	$(P_5/P_4)_f$	
1.4286	2.0001	1.5001	1.5002	1.5002	
Δ_{01}	Δ_{12}	Δ_{23}	Δ_{34}	Δ_{45}	
$4.886 \cdot 10^{-5}$	$6.4261 \cdot 10^{-5}$	$8.2549 \cdot 10^{-5}$	0.00013246	0.00016031	
ϕ_{01}	ϕ_{12}	ϕ_{23}	ϕ_{34}	ϕ_{45}	
$177.0°$	$219.0°$	$195.0°$	$172.0°$	$170.0°$	
A_{01}	A_{12}	A_{23}	A_{34}	A_{45}	
$3.89°$	$0.125°$	$0.0561°$	$0.0538°$	$0.0719°$	
Planet Triplet 012	Planet Triplet 123	Planet Triplet 234	Planet Triplet 345		
ϕ_{012}	ϕ_{123}	ϕ_{234}	ϕ_{345}		
$92.3°$	$277.0°$	$234.0°$	$194.0°$		
A_{012}	A_{123}	A_{234}	A_{345}		
Σ_{1AU}	h	τ_a	Integration Time	Stellar Mass	
$2080 g/cm^2$	0.0991	$123 kyr$	$369 kyr$	$1.02 M_\odot$	

NOTE—Orbital, migration, and MMR parameters for each planet in the example third-order system. Parameters of the planets involved in the third-order resonance are highlighted in red.

Table 4. Frequencies of Individual MMR

Category	Count	Percentage Against Category
First-Order Resonant Pairs	22444	$94.6 \pm 0.1\%$
2:1 MMR	10321	$46.0 \pm 0.003\%$
3:2 MMR	8138	$36.3 \pm 0.003\%$
4:3 MMR	2505	$11.2 \pm 0.002\%$
5:4 MMR	885	$3.94 \pm 0.001\%$
6:5 MMR	381	$1.7 \pm 0.0009\%$
7:6 MMR	113	$0.503 \pm 0.0005\%$
8:7 MMR	50	$0.223 \pm 0.0003\%$
9:8 MMR	37	$0.165 \pm 0.0003\%$
10:9 MMR	10	$0.0446 \pm 0.0001\%$
11:10 MMR	4	$0.0178 \pm 9 \cdot 10^{-5}\%$
Second-Order Resonant Pairs	1124	$4.74 \pm 0.1\%$
3:1 MMR	319	$28.4 \pm 0.01\%$
5:3 MMR	500	$44.5 \pm 0.01\%$
7:5 MMR	196	$17.4 \pm 0.01\%$
9:7 MMR	82	$7.3 \pm 0.008\%$
11:9 MMR	23	$2.05 \pm 0.004\%$
13:11 MMR	2	$0.178 \pm 0.001\%$
15:13 MMR	1	$0.089 \pm 0.0009\%$
21:19 MMR	1	$0.089 \pm 0.0009\%$
Third-Order Resonant Pairs	151	$0.637 \pm 0.05\%$
4:1 MMR	12	$7.95 \pm 0.02\%$
5:2 MMR	27	$17.9 \pm 0.03\%$
7:4 MMR	31	$20.5 \pm 0.03\%$
8:5 MMR	59	$39.1 \pm 0.04\%$
10:7 MMR	14	$9.27 \pm 0.02\%$
11:8 MMR	5	$3.31 \pm 0.01\%$
14:11 MMR	2	$1.32 \pm 0.009\%$
16:13 MMR	1	$0.662 \pm 0.007\%$

NOTE—The number of planet pairs that capture into each mean-motion resonance defined by $p\!:\!q$ observed in our simulations. Uncertainties are estimated from counting statistics.